Eur. Phys. J. A (2011) **47**: 89
DOI 10.1140/epja/i2011-11089-0

THE EUROPEAN PHYSICAL JOURNAL A

Regular Article – Experimental Physics

Quasi-free photoproduction of η-mesons off the deuteron

The CBELSA/TAPS Collaboration

I. Jaegle[1], B. Krusche[1,a], A.V. Anisovich[2,3], J.C.S. Bacelar[4], B. Bantes[5], O. Bartholomy[2], D.E. Bayadilov[2,3], R. Beck[2], Y.A. Beloglazov[3], R. Castelijns[4], V. Crede[6], M. Dieterle[1], H. Dutz[5], D. Elsner[5], R. Ewald[5], F. Frommberger[5], C. Funke[2], R. Gothe[5,8], R. Gregor[7], A.B. Gridnev[3], E. Gutz[2], W. Hillert[5], S. Höffgen[5], P. Hoffmeister[2], I. Horn[2], J. Junkersfeld[2], H. Kalinowsky[2], S. Kammer[5], I. Keshelashvili[1], V. Kleber[5], Frank Klein[5], Friedrich Klein[5], E. Klempt[2], M. Konrad[5], M. Kotulla[1], M. Lang[2], H. Löhner[4], I.V. Lopatin[3], S. Lugert[7], Y. Maghrbi[1], D. Menze[5], T. Mertens[1], J.G. Messchendorp[4], V. Metag[7], V.A. Nikonov[2,3], M. Nanova[7], D.V. Novinski[2,3], R. Novotny[7], M. Oberle[1], M. Ostrick[5,9], L.M. Pant[7,10], H. van Pee[2,7], M. Pfeiffer[7], F. Pheron[1], A. Roy[7,11], A.V. Sarantsev[2,3], S. Schadmand[7,13], C. Schmidt[2], H. Schmieden[5], B. Schoch[5], S.V. Shende[4,12], V. Sokhoyan[2], A. Süle[5], V.V. Sumachev[3], T. Szczepanek[2], U. Thoma[2,7], D. Trnka[7], R. Varma[7,11], D. Walther[5], C. Wendel[2], D. Werthmüller[1], and L. Witthauer[1]

[1] Departement Physik, Universität Basel, Switzerland
[2] Helmholtz-Institut für Strahlen- und Kernphysik der Universität Bonn, Germany
[3] Petersburg Nuclear Physics Institute, Gatchina, Russia
[4] KVI, University of Groningen, The Netherlands
[5] Physikalisches Institut der Universität Bonn, Germany
[6] Department of Physics, Florida State University, Tallahassee, USA
[7] II. Physikalisches Institut, Universität Giessen, Germany
[8] present address: University of South Carolina, USA
[9] present address: University of Mainz, Germany
[10] on leave from Nucl. Phys. Division, BARC, Mumbai, India
[11] on leave from Department of Physics, Indian Institute of Technology Mumbai, India
[12] present address: Department of Physics, University of Pune, Pune, India
[13] present address: Institut für Kernphysik, Forschungszentrum Jülich, Germany

Received: 13 April 2011 / Revised: 23 June 2011
Published online: 1 August 2011 –
Communicated by Z.-E. Meziani

Abstract. Precise data for quasi-free photoproduction of η-mesons off the deuteron have been measured at the Bonn ELSA accelerator with the combined Crystal Barrel/TAPS detector for incident photon energies up to 2.5 GeV. The η-mesons have been detected in coincidence with recoil protons and neutrons. Possible nuclear effects like Fermi motion and re-scattering can be studied via a comparison of the quasi-free reaction off the bound proton to η-production off the free proton. No significant effects beyond the folding of the free cross-section with the momentum distribution of the bound protons have been found. These Fermi motion effects can be removed by an analysis using the invariant mass of the η-nucleon pairs reconstructed from the final-state four-momenta of the particles. The total cross-section for quasi-free η-photoproduction off the neutron reveals even without correction for Fermi motion a pronounced bump-like structure around 1 GeV of incident photon energy, which is not observed for the proton. This structure is even narrower in the invariant-mass spectrum of the η-neutron pairs. Position and width of the peak in the invariant-mass spectrum are $W \approx 1665$ MeV and FWHM $\Gamma \approx 25$ MeV. The data are compared to the results of different models.

1 Introduction

The excitation spectrum of the nucleon is one of the most important testing grounds for our understanding of the strong interaction at the few-GeV scale, where perturbative methods cannot be applied. It plays a similar role for the strong interaction as atomic spectra do for the electromagnetic interaction. However, so far, on the theory side, the only direct connection between baryon properties and Quantum Chromodynamics (QCD) has been established with the numerical methods of lattice gauge theory. The progress in this field was tremendous during the last few

[a] e-mail: Bernd.Krusche@unibas.ch

years for the ground-state properties of hadrons [1]. But only very recently also first results for excited states [2] going beyond earlier quenched approximations [3,4] became available.

In a more indirect way, experimental observations and QCD are connected via QCD inspired quark models. However, in spite of their phenomenological successes, the basis of these models is still not well anchored. There is neither consent about the effective degrees of freedom nor about the residual quark-quark interactions (see *e.g.* ref. [5,6] for detailed reviews). Apart from the standard, non-relativistic quark model with three equivalent valence quarks, also models with a quark-diquark structure (see *e.g.* [7]), algebraic approaches [8], and flux-tube models [9] have been proposed, all with different internal degrees of freedom, giving rise to different excitation schemes. In a radically different picture of hadrons, it was even attempted to generate all excited states by chirally coupled channel dynamics [10], leaving only the ground-state multiplets as genuine qqq states.

So far, comparison of the experimentally known excitation spectrum of the nucleon to model predictions does not clearly favor any of the different models, but reveals severe difficulties for all of them. The ordering of some of the lowest-lying states is not reproduced. In particular, the $N(1440)P_{11}$ ("Roper") resonance and the first excited Δ, the $P_{33}(1600)$, which in the quark model belong to the $N = 2$ oscillator shell, appear well below the states from the $N = 1$ shell. Furthermore, even the models with the fewest effective degrees of freedom predict many more states than have been observed, which is known as the "missing resonance" problem.

Since most states have been observed with elastic scattering of charged pions it is possible that the database is biased towards states that couple strongly to πN. As an alternative, photon-induced reactions, which nowadays can be experimentally investigated with comparable precision as hadron-induced reactions, have moved into focus. In order to avoid bias due to the resonance decay properties, a large effort has been made during the last few years at tagged photon facilities to study many different final states [11,12]. So far, these experiments have mostly concentrated on the free proton. However, data from the neutron is also important, because it reveals the iso-spin composition of the electromagnetic excitation amplitudes. In extreme cases $\gamma N N^\star$ couplings may even be completely forbidden due to $SU(6)$ selection rules [13]. Although due to the non-negligible spin-orbit mixing in the wave functions they are not strictly forbidden in more realistic models, they remain suppressed and can be better studied using neutron targets. Such experiments are of course complicated by the non-availability of free neutrons as targets, requiring coincident detection of recoil neutrons from light target nuclei and reaction models taking into account possible nuclear effects on the observed cross sections.

During the last few years the CBELSA/TAPS Collaboration has started in Bonn an extensive program for the study of quasi-free meson production reactions off the deuteron, including the $n\eta$ [14], $n\eta'$ [15], $n\omega$, $n\pi^0\pi^0$, and $n\eta\pi^0$ final states. These are reactions with only neutrons and photons in the final state, which can only be investigated with highly efficient electromagnetic calorimeters covering almost the full solid angle. In the present paper we discuss the experimental details and analysis procedures and summarize the results for the η-photoproduction. Some results from this reaction have already been presented in a letter [14], the results for the η'-channel have been published recently, and the results from the other channels will be published elsewhere.

2 Quasi-free photoproduction of η-mesons

Photoproduction of η-mesons off the free proton has been previously studied in detail [16–32] from the production threshold at $\approx 707\,\mathrm{MeV}$ up to incident photon energies of 2.8 GeV. In the threshold region this reaction is completely dominated by the photoexcitation of the $S_{11}(1535)$ resonance [33]. A detailed analysis of the angular distributions [16] revealed a small contribution of the $D_{13}(1520)$ via an interference with the leading E_{0^+}-multipole of the S_{11} excitation. The effect is more pronounced for the beam asymmetry measured with linearly polarized photons [17,27,34] and an analysis in the framework of the "Eta-MAID" model [35] allowed the extraction of the tiny $N\eta$ branching ratio $(0.23 \pm 0.04\%)$ [36] of the D_{13} resonance. In the range of the second S_{11} resonance, the $S_{11}(1650)$, all models find a destructive interference between the two S_{11} states. The situation is less clear above this range, where different analyses like Eta-MAID [35] and Bonn-Gatchina (BoGa) [37] propose different resonance contributions (see *e.g.* [27]).

So far, the isospin degree of freedom was almost exclusively explored in the excitation range of the first S_{11} resonance. The results of quasi-free production off the deuteron and ^{4}He with and without detection of recoil nucleons [38–41] are all consistent with

$$\frac{\sigma_n}{\sigma_p} \approx \frac{2}{3}\,, \tag{1}$$

where σ_n and σ_p are the cross-sections for η-photoproduction off neutrons and protons, respectively. The resulting ratio of the helicity couplings $A^n_{1/2}$ and $A^p_{1/2}$ for the $S_{11}(1535)$ is [12]

$$\left|A^n_{1/2}\right| / \left|A^p_{1/2}\right| = 0.82 \pm 0.02. \tag{2}$$

The investigation of coherent η-photoproduction off the deuteron [39,42], ^{3}He [43], and ^{4}He [40], and the comparison of the interference terms in the angular distributions of quasi-free production off the proton and the neutron [41] have shown that the $S_{11}(1535)$ excitation is dominantly iso-vector, so that [12]

$$A^{IS}_{1/2} / A^p_{1/2} = 0.09 \pm 0.01, \tag{3}$$

where $A^{IS}_{1/2}$ is the iso-scalar part of the amplitude.

Previously measured and predicted cross section ratios are summarized in fig. 1. The Eta-MAID model [35] agrees well with the 2/3 ratio in the $S_{11}(1535)$ range, but

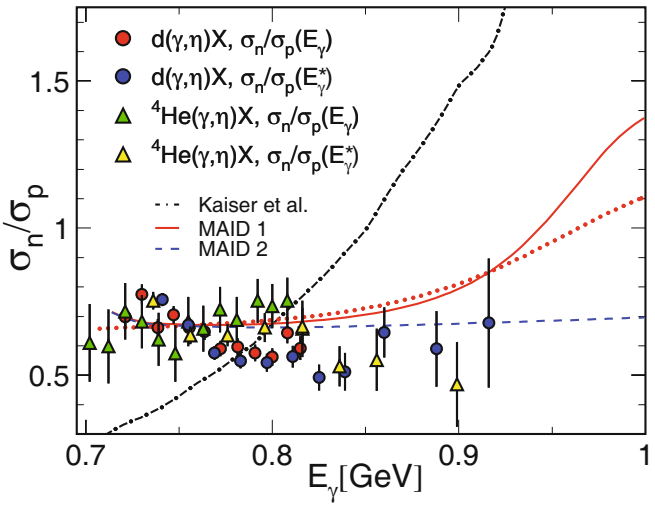

Fig. 1. Comparison of measured σ_n/σ_p ratios from [40,41] to model predictions. Eta-Maid model [35] (MAID 1 (solid curve): full model, dotted curve: full model after folding with momentum distributions of bound nucleons, MAID 2 (dashed curve): only $S_{11}(1535)$ and background). Dash-dotted curve: chirally coupled channel dynamics, Kaiser *et al.* [44,45]. E^*_γ: effective photon energy corrected for Fermi momentum.

predicts for higher incident photon energies a significant rise due to the contributions from other resonances. This effect should still be visible for quasi-free cross-sections measured for nucleons bound in the deuteron, which is demonstrated by the dotted curve in fig. 1. The largest contribution to the rise comes in this model from the $D_{15}(1675)$ resonance, which is one of the states which due to the Moorehouse selection rules [13] should have much larger electromagnetic couplings to the neutron than to the proton. However, the $N\eta$ branching ratio of this state was determined in the model from a fit to the proton data as 17%. This rather large value is in conflict with other results; PDG [36] gives only an upper limit of $< 1\%$.

A strong rise of the ratio to higher incident photon energies was also predicted in the framework of a chiral coupled channel model by Kaiser and collaborators [44, 45]. But in this case the rise is not related to the contribution of higher-lying resonances, it is related to the properties of the $S_{11}(1535)$, which in this model is not interpreted as a genuine qqq state but as a dynamically generated $K\Sigma$-molecule–like state.

Finally, also in the framework of the chiral soliton model [46,47] a state was predicted in this energy range, which has a much stronger photon coupling to the neutron than to the proton *and* a large decay branching ratio into $N\eta$. This state is the nucleon-like member of the conjectured antidecuplet of pentaquarks, which would be a P_{11} state. Exact $SU(3)_F$ would forbid the photo-excitation of the proton to the proton-like member of the antidecuplet. But even after accounting for $SU(3)_F$ violation the chiral soliton model predicts [46] that the photo-excitation of this state is suppressed on the proton and should mainly occur on the neutron. Kim *et al.* [48] have calculated the magnetic transitions moments for the antidecuplet states and found a considerable enhancement for the excitation of the nucleon-like state on the neutron with respect to the proton.

Strong efforts have recently been undertaken at various facilities (GRAAL in Grenoble [49], ELSA in Bonn [14] and LNS in Sendai [50]) to extract reliable results for the $\gamma n \to n\eta$ reaction at higher incident photon energies. The somewhat unexpected finding in all experiments is not only a significant rise of the cross-section on the neutron with rising incident photon energy, but a fairly narrow peak in it, which has no counterpart in the reaction off the proton.

The nature of this structure is still unknown and many different suggestions have been put forward in the literature. They include various types of coupled channel effects involving known nucleon resonances [51,52] or the opening of production thresholds [53], but also scenarios with contributions from intrinsically narrow states have been discussed [54,55]. Very recently, Kuznetsov *et al.* [56] have reported a narrow structure in Compton scattering off the quasi-free neutron with a similar mass and width, although not with large statistical significance ($\approx 4.6\sigma$). Such an observation would make explanations with complicated interference and threshold effects less likely since there is no good reason why they should appear similar for such different reactions. A nucleon resonance with strong photon coupling to the neutron, on the other hand, naturally would be expected to show up also in Compton scattering off the neutron.

In this paper, we will summarize and discuss in detail the results from the ELSA experiment reported partly in [14] and in addition present a new analysis which removes the effects of Fermi motion from the data through a kinematic reconstruction of the involved nucleon momenta. In this way, more stringent constraints can be put on the intrinsic width of the peak-like structure.

The paper is organized in the following way. The experimental setup is described in sect. 3. Details of the analysis are discussed in sect. 4. This includes the calibration of all detector components, the identification of photons, reconstruction of mesons, and detection of recoil nucleons, the absolute normalization of the cross-sections and a thorough discussion of systematic uncertainties. The results are summarized in sect. 5. We first compare the data to previous results from quasi-free photoproduction off the deuteron and the results for the quasi-free proton to free proton data. In the following two subsections the results for quasi-free photoproduction are first discussed in dependence of the incident photon energy. In this analysis the width of narrow structures is dominated by nuclear Fermi motion. In a second analysis results are constructed in dependence of the nucleon-meson invariant mass in the final state calculated from the four vectors of the observed particles. In this way, Fermi motion effects are removed and only instrumental resolution must be considered.

3 Experimental setup

The experiment was performed at the electron stretcher accelerator facility ELSA in Bonn [57,58], which can de-

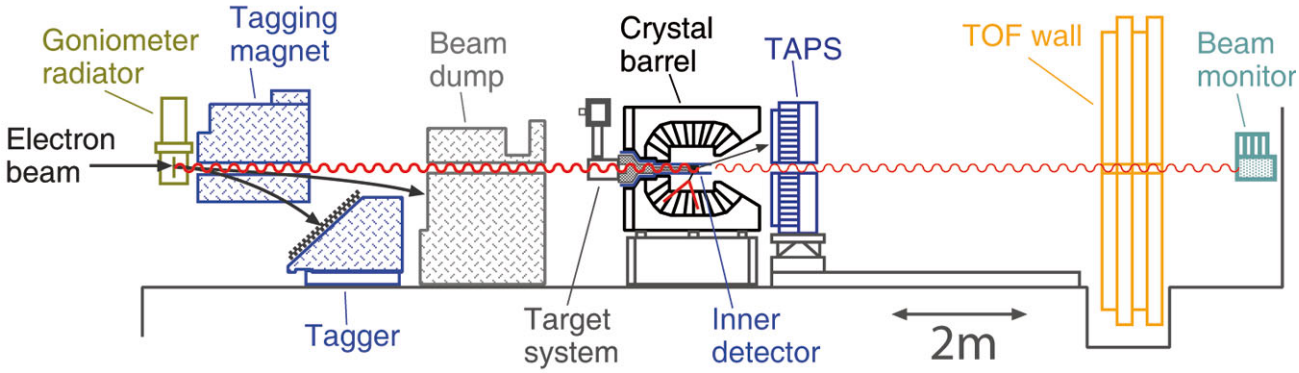

Fig. 2. Overview of the experimental setup. The electron beam enters from the left side. Scattered electrons were detected in the counters of the tagging spectrometer (cf. fig. 3). The liquid deuterium target was mounted in the center of the Crystal Barrel. The forward range was covered by the TAPS detector. The time-of-flight wall was mounted, but not used in the experiment. Beam intensity was monitored at the end of the beam line.

liver electron beams with intensities of a few nA for energies up to 3.5 GeV. The overall setup of the experiment is shown in fig. 2. The incoming electron beam is impinging on the radiator mounted in a goniometer. For the measurement discussed here, electron beam energies of 2.6 GeV and 3.2 GeV were used. The largest part of the 3.2 GeV beam time was done with a copper radiator foil of 0.3% radiation lengths thickness, producing unpolarized bremsstrahlung. For the rest of this beam time and for the beam times with 2.6 GeV electron energy a diamond radiator was used to produce coherent bremsstrahlung with maximum linear polarization around 1 GeV incident photon energy (see [59] for details about linear polarization of the photon beam).

Electrons which have emitted bremsstrahlung, are then deflected downwards by a dipole magnetic field onto the focal plane of the tagging system, where energy and timing information is extracted. Unscattered electrons are stopped in the beam dump. The bremsstrahlung photons are almost co-linear with the incident electron beam, pass through a hole in the magnet yoke and irradiate the liquid deuterium target mounted in the center of the Crystal Barrel detector. The core of the detector system of the tagging spectrometer (see fig. 3) are 14 partially overlapping plastic scintillator bars each with photo-multipliers at both ends. This system covers 22% to 92% of the incoming electron beam energy E_0. A second layer has been added in front of the bars for better energy resolution. A scintillating fiber detector (2×240 fibers arranged in two layers to partly overlap) covers photon energies from 18% to 80% of E_0. This defined the maximum tagged photon energy of 2.5 GeV. The fiber detector provides an energy bin width of $\approx 1.5\%$ for the lowest incident photon energies and $\approx 0.1\%$ at the high energy. In principle, the range from 80% to 92% of E_0 can be tagged with an additional wire chamber. The chamber was, however, not used in the present experiment since due to the small cross-section the statistical quality of data in this range was not sufficient.

The target consisted of a vertically mounted cryostat attached to a tube entering the Crystal Barrel detector from the upstream side. The target cell itself was a cap-

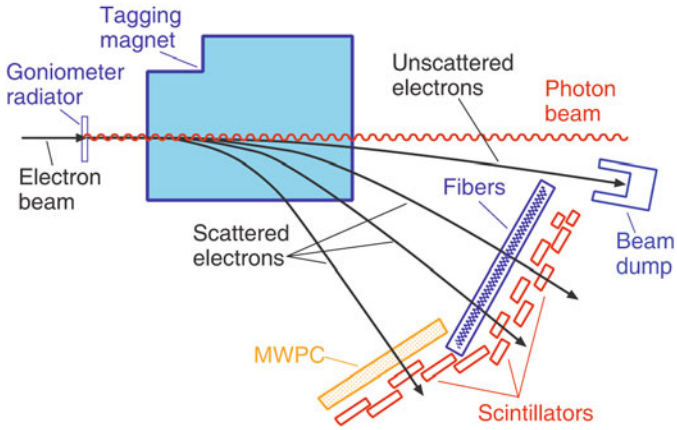

Fig. 3. Setup of the tagging spectrometer. Unscattered electrons stop in the beam-dump. Scattered electrons pass a two-layer detection system. Scintillating fiber detectors (good position resolution) and scintillator bars (good time resolution) cover photon energies up to 80% of the electron beam energy. The part covered by a multiple wire chamber (MWPC) (low-energy electrons corresponding to photon energies above 80% of the electron beam energy) was not used in the experiment.

ton cylinder (0.125 mm foil thickness) with a diameter of 3 cm and length of 5.275 cm, filled with liquid deuterium (surface thickness 0.26 nuclei/barn).

Reaction products emerging from the target have been detected with a combined setup (see fig. 4) of the Crystal Barrel detector [60] and the TAPS detector [61,62]. In the configuration used, the Crystal Barrel consisted of 1290 CsI (Tl) crystals of 16 radiation lengths X_o all mounted in a target pointing geometry. It covered the full azimuthal angle for polar angles between 30° and 168°. The forward angular range was covered by the TAPS detector [61,62]. This component was made of 528 BaF_2 crystals of hexagonal shape with an inner diameter of 5.9 cm and a length of 25 cm corresponding to 12 X_o. They were arranged in a wall-like structure as shown in the lower part of fig. 4, covering polar angles down to 4.5°. The front face of the BaF_2 wall was located 1.18 m from the center of the target.

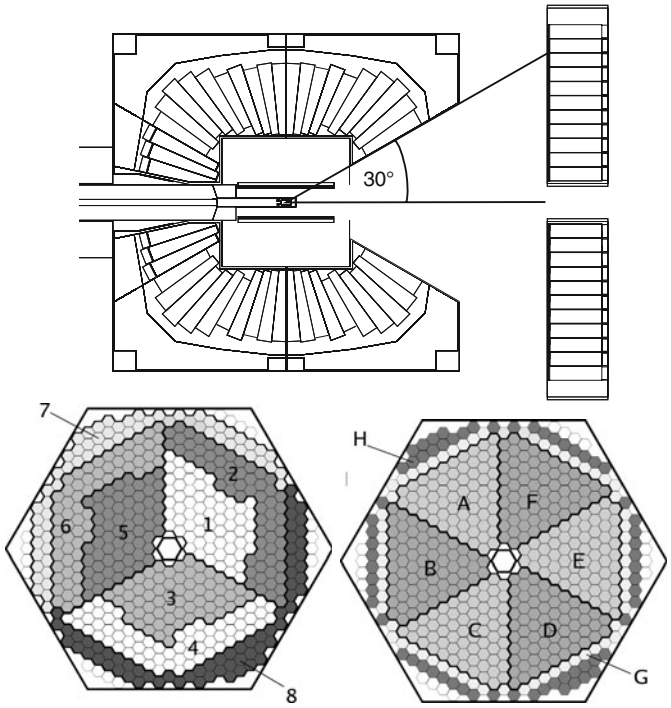

Fig. 4. Arrangement of the Crystal Barrel and TAPS detectors. Upper part: side view, lower part: front view of the TAPS wall: left-hand side: logical segmentation for the LED-low trigger, right-hand side: logical segmentation for the LED-high trigger (see text).

The two calorimeters have a comparable energy resolution [60,62]

$$\frac{\sigma_E}{E} \approx \frac{2\text{–}3\%}{\sqrt[4]{E/\mathrm{GeV}}}\,. \tag{4}$$

Since the impact points of photons are determined from the center of gravity of the electromagnetic showers, the angular resolution is better than the granularity of the crystals. It is 1.5° (σ) for the Crystal Barrel [60] for photons with energies above 50 MeV and 1.25° in TAPS. Angular resolution for recoil nucleons, which do not produce extended clusters, is closer to the granularity.

Both parts of the calorimeter were equipped with detectors for the identification of charged particles. A three-layer scintillating fiber detector ("Inner"-detector) [63] was mounted inside the Crystal Barrel around the target, covering polar angles between 28° and 172°. The outer layer (diameter 12.8 cm, 191 fibers) runs parallel to the z-axis. The middle layer ($\varnothing$ = 12.2 cm, 165 fibers) is wound anti-clockwise at an angle of 25° with respect to the z-axis and the inner layer ($\varnothing$ = 11.6 cm, 157 fibers) is wound clockwise at 25°. All fibers have 2 mm diameter. This orientation allows the reconstruction of the spatial coordinates of the intersection point of the charged particle trajectory with the detector (see [64] for details). The TAPS detector was complemented with a charged-particle-veto (CPV) detector built of 5 mm thick plastic scintillators of hexagonal shape and the same dimensions as the front-face of the BaF_2 crystals, so that each detector module had its individual veto detector. The CPV was read out by wavelength shifting fibers connected to multi-anode photo-multipliers.

The fast BaF_2 modules of the TAPS detector were read out by photo-multipliers, but the CsI crystals of the Barrel were read by photo-diodes, which do not provide any time information. This had important consequences for the hardware trigger. Signals for the first-level trigger could only be derived from the TAPS detector. For this purpose each module was equipped with two independent leading-edge discriminators, combined in two different ways into logical groups (see fig. 4). For most of them (ring 12–5 from outer edge to center) a lower threshold was set to $\approx$ 55 MeV (LED-low). It was set to 80 MeV, 135 MeV, 270 MeV for rings 4, 3, 2, respectively. The innermost ring was not used in the trigger. The LED-high thresholds were set to 70 MeV for rings 9–7, rising from 105 MeV (ring 6) to 180 MeV (ring 2). Again, the innermost ring was not used in the trigger and the three outer rings (block G) had no leading edge discriminators for the high threshold. The first-level trigger then included two components: at least two LED-low discriminators from different logical sectors above threshold, or at least one LED-high discriminator above threshold. In the second case, a second-level trigger from the FAst Cluster Encoder (FACE) of the Crystal Barrel, indicating at least two separated hits in the Barrel, was required in addition. All first level triggers thus required detection of one or two photons in TAPS, which covered only a small part of the solid angle. Therefore, only reactions with relatively high photon multiplicity like $\gamma d \to np\pi^0\pi^0 \to np4\gamma$, $\gamma d \to np\eta \to np3\pi^0 \to np6\gamma$, or $\gamma d \to np\eta' \to np\eta 2\pi^0 \to np6\gamma$ could be recorded. Two-photon decays of single meson production reactions like $\gamma d \to np\pi^0 \to np2\gamma$ or $\gamma d \to np\eta \to np2\gamma$ were not taken. It should be mentioned that this restriction of the detector setup applies only to reactions off the (quasi)-free neutron. In measurements off the free proton, the recoil protons provide trigger signals from the Inner-detector (or TAPS). The TAPS modules were additionally equipped with constant fraction discriminators (CFD), with thresholds around 10 MeV, which were used for the high-resolution measurement of the time and generated the read-out pattern of the detector matrix.

The last component of the setup is the so-called γ-veto detector at the end of the photon-beam line, which consisted of nine lead-glass crystals, and counted the photons which passed through the target without interaction. It was used to monitor the time dependence of the photon-beam intensity. Furthermore, it was used to measure the tagging efficiency, *i.e.* the fraction of photons, correlated with electrons, which impinged on the target. This was done in special tagging efficiency runs, where at reduced beam intensity the tagger was used as trigger and the number of scattered electrons counted in the tagger was compared to the number of coincident photons impinging on the γ-veto.

4 Data analysis

In this chapter we discuss the different analysis steps of the experiment, from the most basic calibration procedures for

the different detector components, over the identification of photons and particles, the identification of specific reaction channels, to the absolute normalization of cross-sections. Although in this paper only final states with η-mesons are discussed, a large part of this chapter applies also to the other, simultaneously measured reactions, which will be reported elsewhere. Therefore we discuss in this paper the analysis steps in some detail also in view of possible systematic uncertainties. A full account of all analysis procedures is given in [65].

4.1 Calibration procedures

4.1.1 Tagging system

The tagging system has two tasks: the event-by-event definition of the incident photon energy via a coincidence between the focal plane detectors and the reaction detector and the monitoring of the photon flux from the counting of the deflected electrons.

For the present analysis energy and timing information was obtained with the scintillating fiber detector. Since for any scattered electron the bending radius ρ in the magnetic field B is related to its momentum p by

$$\rho = \frac{p}{Bq}\,, \tag{5}$$

where q is the electron charge, its energy follows from the position in the focal plane detector, *i.e.* the number of the responding fiber. The energy calibration of the scintillating fiber detector was done in two steps. As a starting point a polynomial calibration function was calculated from the measured field map of the dipole magnet and the positions of the scintillating fibers. Initially, this calibration was done for an electron beam energy of 3.2 GeV. For other beam energies, the magnetic field was adjusted such that the unscattered electrons always followed the same trajectory so that the calibration function could be simply scaled by the electron beam energy. This calibration was checked by direct injection of a very low intensity electron beam with removed radiator. At a fixed magnetic field setting for 3.2 GeV ($B = 1.413$ T) ELSA beams with four different energies (1.2, 1.5, 2.0, 2.5 GeV) were used.

A further cross check was done with the position of the peaks from coherent bremsstrahlung produced in a diamond crystal, which was used for measurements with linearly polarized photon beams. The systematic uncertainty of this calibration is on the order of the energy bin widths of the fiber detector.

The measurement of the relative timing between the scattered electrons and the reaction products was done with the focal plane scintillating fiber detector and the TAPS detector. The modules of both detector systems are equipped with individual TDCs. In case of the focal plane detector the start signal came from the individual fibers and the stop from the trigger signal. The TAPS TDCs were started with the trigger signal and stopped by the individual CFD signals. The time calibration of the tagger TDCs was 64 ps/channel. After alignment of all channels a time resolution of 1.6 ns (FWHM) was achieved for the sum spectrum, which is shown in fig. 5. The average multiplicity of hits in the focal plane detector per event in the coincidence time window of 460 ns was $\approx$ 20, resulting in a significant random background. After a cut on the prompt peak ($\pm$3 ns), the remaining background corresponding to region B in fig. 5 was removed from all shown spectra in the usual way by subtraction of the events from the areas D and C normalized by the ratio of the areas B/(D+C). The random background was much less important for events with photons from an identified η-meson (dashed histograms in fig. 5). Also the small asymmetric tail of the prompt peak (cf. fig. 5), due to particles misidentified as photons, vanishes in this case.

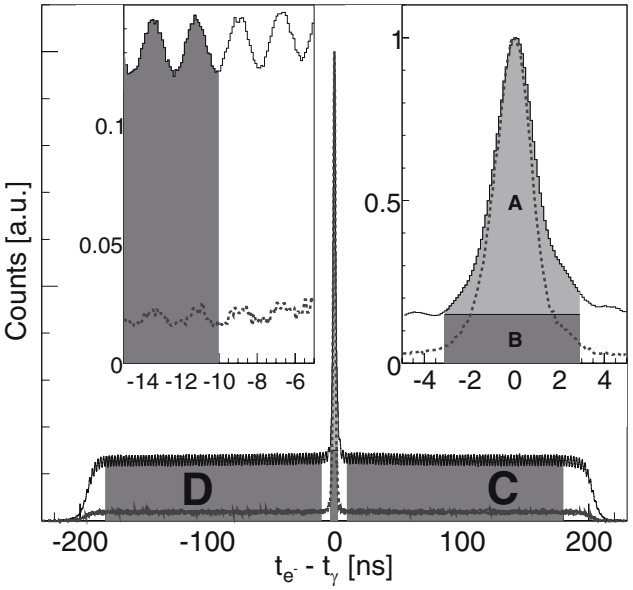

Fig. 5. Relative TAPS-tagger time spectrum for all events with photons in TAPS (solid histograms) and for events with η-decay photons in TAPS (dashed histograms). The 2 ns time structure of the beam is reflected in the fine structure of the accidentals. The shaded areas indicate the prompt (A) and random (B, C, D) coincidence areas (see text).

4.1.2 TAPS

A precise calibration of the time measurement with TAPS was not only important for the suppression of random background. It was also the basis of the measurement of the kinetic energy of recoil nucleons with the time-of-flight method. The slightly varying gaines of the TDCs were measured for each channel with pulser signals of known delay, fed into the electronic chain. The alignment of all channels was done with events with two or more photons detected in TAPS. For this procedure, photons were identified with the help of the veto detector and an invariant-mass analysis, which accepted only decay photons of π^0-mesons. The resulting TAPS-TAPS coincidence time spectrum had a resolution of 650 ps (much better than the TAPS-tagger timing) and a peak-to-background ratio of 100.

The energy calibration was done in three steps. In the first step the energy deposition of minimum ionizing cosmic myons ($\approx 38.5\,\mathrm{MeV}$) were used for a relative calibration of all detector modules. Such a calibration does not take into account differences in the detector response to the energy deposition of myons and electromagnetic showers as well as shower leakage. Therefore, in the second step the linear term of the calibration was adjusted for all modules in an iterative procedure with the invariant-mass peak of π^0-mesons. In the third step, a quadratic correction of the energy calibration was introduced using the position of the invariant mass peak of the η-meson. A final accuracy of $\pm 1\%$ for the position of the π^0- and η-peaks was achieved. More details can be found in [65].

4.1.3 Crystal Barrel

Due to the read-out with photo-diodes, the CB delivers only energy information. A calibration with cosmic myons is not practical, due to the different geometries and orientations of the individual modules. The digitization of the detector signals is done for two different dynamic ranges. The calibration for the low-gain chain was again done with an iterative procedure using the π^0 invariant mass peak. The high-gain branch was calibrated by the injection of laser light of known intensity into the crystals.

4.2 Identification of particles and reaction channels

Electromagnetic showers, depending on their energy, will in general produce signals in an extended "cluster" of scintillator modules. In a first step of the analysis all hits in the calorimeters were grouped into "clusters" of adjacent crystals and the energy sums and geometrical centers of gravity of the "clusters" were extracted (see [64] for details). In the next step, the TAPS-veto detector and the Inner-detector were used to separate neutral hits (photon and neutron candidates) from charged hits (proton candidates) in the detectors. In TAPS a hit was assigned to "charged" if the veto of any module from the cluster or the veto of any neighbor of the central module of the cluster had fired (even if the neighbor module itself had no signal above threshold). The latter condition is important for charged particles with relatively large impact angles which may traverse the edge of a veto but deposit their energy in the neighbor module. All other hits were assigned to "neutral". In the Barrel, a hit was assigned to "charged", if at least two layers of the Inner-detector had recorded a hit within $\pm 10^\circ$ of azimuthal angle. The efficiency of the Inner-detector for this condition is 98.4% [63]. It was assigned to "neutral" if no layer had fired within this azimuthal angle, which results in a probability of $\approx 0.04\%$ to misidentify a charged particle as neutral hit. Events with hits with one responding layer of the Inner-detector were discarded.

After these assignments three partly overlapping classes of events were included into the analysis. Class (a) included events with exactly six neutral hits and exactly one charged hit. Class (b) included events with exactly seven neutral hits and no charged hit (in this case it was additionally required that the Inner-detector had not fired at all). Class (c) included all events from classes (a) and (b) and in addition all events with exactly six neutral hits and no charged hit. Class (a) corresponds to quasi-free production off the proton $\gamma d \rightarrow (n)p\eta$ with coincident detection of the recoil proton. Class (b) corresponds to quasi-free production off the neutron $\gamma d \rightarrow (p)n\eta$ with coincident detection of the recoil neutron. Class (c) corresponds to the inclusive reaction $\gamma d \rightarrow (np)\eta$, without any condition for the recoil nucleon (may be detected but is not required).

These events were subjected to a combined invariant and missing-mass analysis. In the first step of the invariant-mass analysis the invariant masses of all combinations of three disjunct pairs of neutral hits were calculated. In the case of six neutral hits (events with proton candidate or without candidate for recoil nucleon) these are 15 different combinations among which the "best" combination was chosen by a χ^2-test, minimizing

$$\chi^2 = \sum_{k=1}^{3} \frac{(m_k(\gamma\gamma) - m_{\pi^0})^2}{(\Delta m_k(\gamma\gamma))^2} \tag{6}$$

for all disjunct combinations where m_{π^0} is the pion mass and the $m_{\gamma\gamma}$ are the invariant masses of the photon pairs with their uncertainties $\Delta m_{\gamma\gamma}$ calculated for each photon pair from the energy and angular resolution of the detector. For events with seven neutral hits (events with neutron candidate) one must in addition loop over the un-paired hit giving rise to 105 combinations. Once the "best" combination was determined, in all cases a cut between 110 MeV and 160 MeV was applied to the invariant masses. Only events where all three pairs of the best combination passed this cut were kept. Subsequently, for events with seven neutral hits, the residual hit was taken as neutron candidate.

The nominal mass of the pion was then used to improve the experimental resolution. Since the angular resolution of the detector is much better than the energy resolution this was done by re-calculating the photon energies and momenta from the approximation

$$E'_{1,2} = E_{1,2} \frac{m_{\pi^0}}{m_{\gamma\gamma}}\,, \tag{7}$$

where $E_{1,2}$ are the measured photon energies, $E'_{1,2}$ the re-calculated energies, m_{π^0} is the nominal π^0 mass, and $m_{\gamma\gamma}$ the measured invariant mass. The slow $E^{-1/4}$ energy dependence of σ_E/E from eq. (4) has been neglected here.

In the last step, the invariant mass of the six hits assigned as photons was calculated. The result is shown in fig. 6 (left-hand side) for three different ranges of incident photon energy. The figure shows the most difficult case for events with neutron candidates, where combinatorial background in the χ^2 analysis of the best combination is higher than for events with six neutrals only.

After the invariant-mass analysis all events were subjected to a missing-mass analysis, where the recoil nucleon,

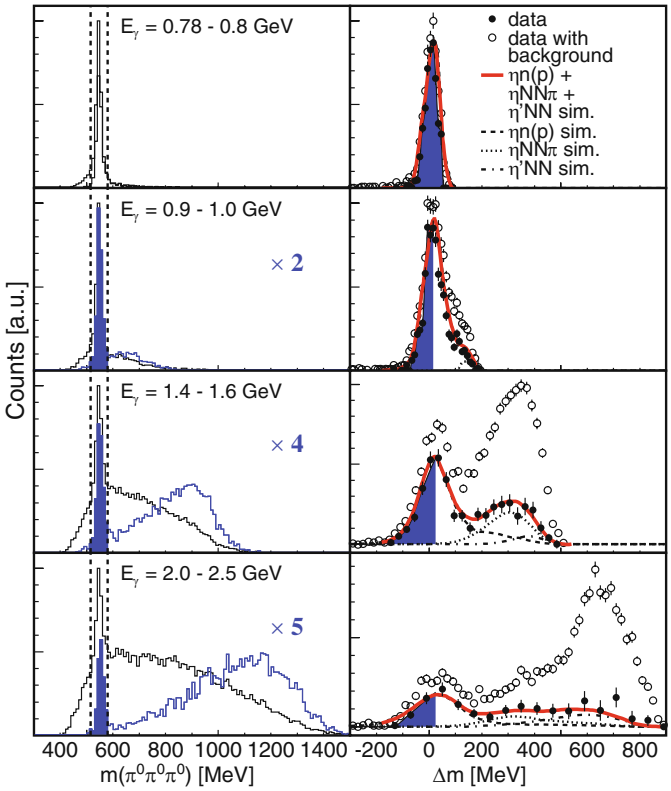

Fig. 6. Invariant (left-hand column) and missing mass (right-hand column) spectra for η-mesons in coincidence with recoil neutrons for three ranges of incident photon energy. Invariant masses: shaded (blue) signal after missing mass cut (scaled up by indicated factors). Dashed lines: applied invariant mass cut. Missing mass data: open symbols represents data for indicated cut on invariant mass. Black dots: background subtracted by fitting invariant-mass spectra for each bin of missing mass. Simulations: dashed (dotted, dash-dotted) curves: simulation of η ($\eta\pi$, η') final states. Solid (red) curves: sum of simulations. Shaded (blue) areas: accepted events.

no matter if a candidate was detected or not, was treated as missing particle. The missing mass Δm of the reaction was calculated for quasi-free production of η-mesons off nucleons via

$$\Delta m = |\mathbf{P}_\gamma + \mathbf{P}_N - \mathbf{P}_\eta| - m_N, \qquad (8)$$

where m_N is the nucleon mass, $\mathbf{P}_\gamma$, $\mathbf{P}_N$, $\mathbf{P}_\eta$ are the four-momenta of the incident photon, the initial-state nucleon (assumed to be at rest), and the produced η-meson. The resulting distributions peak around zero. They are somewhat broadened by the momentum distribution of the bound nucleons, which was neglected. Typical results are shown on the right-hand side of fig. 6. The open symbols correspond to the data after the cuts on invariant mass shown on the left-hand side of the figure have been applied. At higher incident photon energies background in particular from $\eta\pi$ final states is visible, where the pion has escaped detection. A smaller background at the highest incident photon energies is due to the $\eta' \to \eta\pi^0\pi^0$ decay. Cleaner results are obtained when the invariant-mass spectra are generated for each bin of missing mass

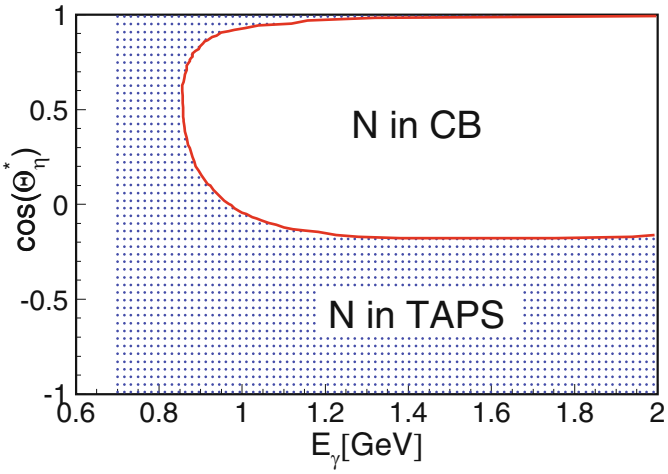

Fig. 7. Simulated distribution of recoil nucleons depending on incident photon energy and η cm polar angle. Nucleons corresponding to the (blue) shaded area are emitted into the solid angle covered by TAPS, nucleons from the white area into the Barrel. Due to Fermi smearing the borders are not sharp.

and fitted with the η line shape and a background polynomial. This analysis demonstrates (compare open and filled symbols in fig. 6, right-hand side) that the background underneath the η invariant-mass peak contributes mainly to large missing masses. Only a small contribution from triple π^0 production appears in the missing mass peak region. The shape of the missing-mass structures for the η, $\eta\pi$, and η' final states has been generated with a Monte Carlo simulation (see below). The sum of these contributions reproduces the measured spectra.

The final analysis was done in the following way. For incident photon energies below 800 MeV, where the reaction $\gamma d \to \eta\pi X$ is kinematically forbidden and the missing-mass spectra are background free, the signals were obtained by fitting the invariant-mass spectra with peak shape and background polynomial. At higher incident photon energies, where background is no longer negligible, first a cut on missing mass was applied, which only accepted events on the left-hand side of the peak (blue shaded areas in fig. 6, right-hand side). The corresponding invariant mass spectra are shown on the left-hand side of the figure as (blue) shaded histograms. The small residual background underneath these invariant mass peaks was fitted and removed. This analysis was done for each bin of incident photon energy and η center-of-momentum (cm) polar angle ($\Theta^\star_\eta$). The missing-mass cut was chosen very restrictive, at the price of the loss of half the counting statistics. This was done to exclude any background contamination, which could create artificial structures in the excitation function around 1 GeV where the background in the missing mass spectra starts to appear.

Finally, we discuss the assignment of recoil nucleons to the events. Figure 7 shows which recoil nucleons need to be detected in TAPS and which in the Barrel, depending on the reaction kinematics. For incident photon energies below $\approx$ 850 MeV all recoil nucleons are emitted into the solid angle covered by TAPS. At higher energies

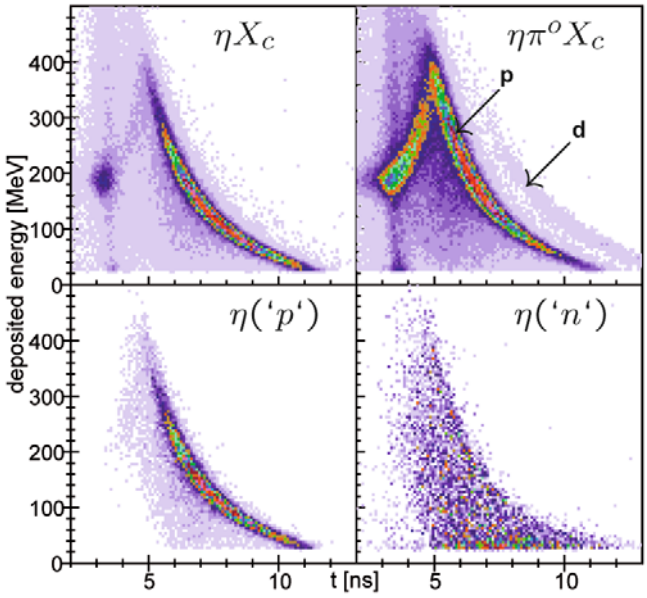

Fig. 8. Time-of-flight *versus* energy spectra measured with TAPS for different event types. Upper left: $\eta \to 6\gamma$ plus one charged particle, upper right: $\eta \to 2\gamma$ and $\pi^o \to 2\gamma$ plus one charged particle, lower left: $\eta \to 6\gamma$ plus one charged particle ("p") and missing-mass cut, lower right: $\eta \to 6\gamma$ plus one neutral particle ("n") and missing-mass cut.

only nucleons corresponding to backward emission of the η-mesons (approximately $\cos(\Theta^\star_\eta) < -0.2$) are detected in TAPS.

Nucleons detected in the Barrel are identified as protons or neutrons as discussed above with the help of the Inner-detector. Due to the three-layer structure of this device the probabilities to misidentify a proton as neutron or vice versa are negligible. Charged pions might be also misidentified as protons. However, such events are reliably removed by the missing mass cut since they originate from $\eta\pi$ final states.

In the case of the TAPS detector, which was placed 1.18 m downstream from the target, an independent check of the recoil nucleon identification was done via a time-of-flight *versus* energy analysis of the recoil particles. This is illustrated in fig. 8. In the spectrum of charged recoil particles detected in coincidence with an η-meson identified by invariant mass (upper left corner) a clear proton band is visible. After the missing-mass cut (lower left corner) almost all background is removed. The spectrum of neutron candidates after application of η invariant- and missing-mass cut (lower right corner) does not show any significant trace of the proton band. The maximum contamination of the TAPS neutron sample by recoil protons was estimated from these spectra to be below 3% (Monte Carlo simulations indicate a maximum contamination at the 4% level). Finally, for the $\eta\pi^0$ final state (upper right corner), which is not further discussed in the present paper, also a clear band for recoil deuterons is visible. This band is missing for the η final state since coherent production of single η mesons off the deuteron is strongly suppressed [42].

Table 1. Summary of beam times. E_{e^-}: electron beam energy, E_{γ_t}: maximum energy of tagged photons, E_{pol}: energy of maximum linear photon beam polarization, Φ_o: energy integrated electron flux on the tagging detectors. Total life time: beam time multiplied by acquisition lifetime fraction.

characteristics	A	B	C	D	E
E_{e^-} [GeV]	2.6	2.6	3.2	3.2	3.2
E_{γ_t} [GeV]	2.0	2.0	2.5	2.5	2.5
E_{pol} [GeV]	1.0	1.0	unpol.	1.2	1.6
total life time [h]	138	18	189	25	25
Φ_o [$10^7 e^-$/s]	1.75	1.6	1.6	2.8	2.8

4.3 Determination of cross-sections and systematic uncertainties

The extraction of cross-sections from the analyzed yields requires several pieces of information: the $\eta \to 6\gamma$ decay branching ratio, the target surface density, the incident-energy–dependent photon flux, and the detection efficiency of the combined Crystal Barrel-TAPS calorimeter with particle identification detectors for photons, protons, and neutrons including all analysis cuts.

The decay branching ratios for $\eta \to 3\pi^0$ and $\pi^0 \to 2\gamma$ are taken from the Particle Data Group [36] as $(32.56 \pm 0.23)\%$ and $(98.823 \pm 0.034)\%$, respectively, resulting in a total branching ratio of 31.42% with a negligible systematic uncertainty. The target surface density (5.3 cm long liquid-deuterium target, density $\rho \approx 0.169\,\mathrm{g/cm^3}$) was 0.26 deuterons/barn with a systematic uncertainty of $\approx 2\%$.

The determination of photon flux and detection efficiency are discussed in detail in the following sub-sections.

4.3.1 Flux normalization

The data have been taken in five blocks of beam time with different electron beam energies and settings of linear beam polarization, which we label A, B, C, D, E. They are summarized in table 1. Due to these settings the statistical quality of the data is less good above 2 GeV incident photon energy.

The photon flux was determined in the following way. The number of scattered electrons detected by the tagger focal plane counters (scintillating fibers) was determined with scalers. The scalers were not life time gated, but the experiment dead time (typically 40%) was recorded with separate scalers and corrected. Due to an electronics/data acquisition problem the scaler information was incorrectly handled for part of the data. This resulted in a loss of the absolute normalization for the beam time blocks B, D, and E, which, however, represent only a minor part of the total statistics. In order to recover the total available statistics, these three data blocks were relatively normalized to the data sets A, C, using the total cross sections for inclusive η-production and double π^0 production.

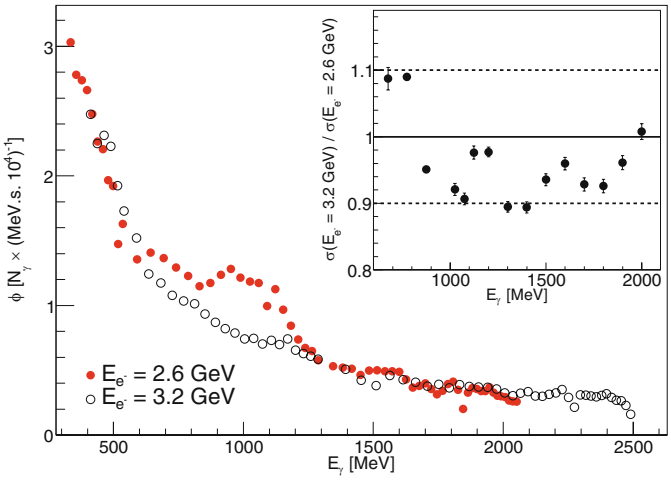

Fig. 9. Main figure: incident photon flux for beam time A (red dots) and beam time C (open black circles). Insert: ratio of inclusive η-photoproduction cross-sections for the two beam times.

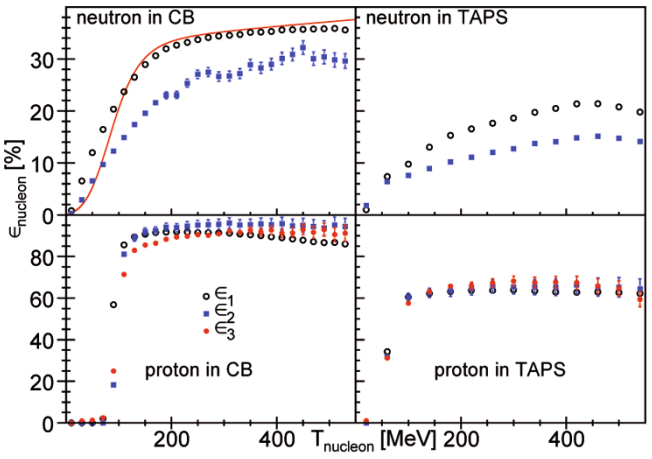

Fig. 10. Detection efficiency for recoil nucleons. Upper row: neutrons, lower row protons, left-hand side: Crystal Barrel, right-hand side: TAPS. For all figures: ϵ_1 (open black circles): MC simulation for isotropically emitted nucleons without further detector hits, ϵ_2 (blue squares): simulation with six decay photons from η-meson decays, ϵ_3 (red dots): experimentally determined proton detection efficiency from η and $2\pi^0$ photoproduction from proton (hydrogen) target (see text). Solid (red) line: measured neutron detection efficiency for CB at CERN [69].

The absolute normalization furthermore requires the measurement of the fraction of correlated photons that impinge on the target. This was done with special tagging efficiency runs, where the intensity of the photon beam was directly measured at the end of the beam line at reduced electron beam intensity. The average tagging efficiency, which is rather flat as function of beam energy, was $\approx 95\%$ for beam time A and $\approx 75\%$ for beam time C (for the latter the beam quality was less good).

The photon flux, *i.e.* the product of the spectrum of electron scalers throughout the tagger detector and the tagging efficiency, for beam times A and C are compared in fig. 9. The overall shapes follow the typical $1/E_\gamma$ behavior of bremsstrahlung. For beam time A the peak from coherent bremsstrahlung is visible around 1 GeV photon energy. The visible structures are due to systematic effects of individual tagger counters. They are also present in the extracted yields and cancel in the cross-sections. The insert shows the ratio of the total cross-sections for inclusive η-photoproduction obtained with the respective photon fluxes for beam times A and C. For most of the energy range systematic deviations are between 0% and −10%. At the lowest incident photon energies they are around +10%. For the measurement with the 3.2 GeV electron beam, this energy region corresponds to the very edge of the tagged range, where systematic uncertainties tend to be larger. For the final result all data sets were averaged according to their statistical weights and a systematic photon flux uncertainty of 10% was estimated.

4.3.2 Monte Carlo simulations and detection efficiency

The detection efficiency of the Crystal Barrel-TAPS setup was modelled with Monte Carlo simulations based on the GEANT3 package [66]. The simulations include all relevant properties of the calorimeter, including geometrical acceptance, charged particle identification, trigger efficiency, response of all detector modules, and analysis cuts. They include also information about inefficient or malfunctioning individual detector modules. This means that the extracted detection efficiencies are effective ones, which cannot be directly applied to data sets taken under different conditions. As far as photon detection and identification of η-mesons via the $\eta \to 3\pi^0 \to 6\gamma$ decay chain are concerned, some details are already given in [67], which used an identical setup for the study of η-photoproduction from heavy nuclei. However, here in addition the detection efficiency for recoil nucleons plays a crucial role. The simulations were done with the GEANT-CALOR program package [68], which is optimized for hadronic interactions from the few MeV to several GeV range, including the interactions of low energy neutrons.

The results for the recoil nucleon detection efficiencies are summarized in fig. 10. For both, neutrons and protons, in the first step isotropically distributed nucleons were simulated. The detection efficiency was determined as a function of kinetic energy T and laboratory polar angle Θ. As expected, angular dependencies of the efficiency (not shown) are negligible for the CB apart from the very edge of the detector. They are more important in the TAPS detector (changing angle of incidence towards the outer edge, increasing discriminator thresholds towards the beam pipe). Figure 10 (black open circles) shows the kinetic energy dependence of the detection efficiency obtained with this simulation, averaged over the polar angle range of the detectors.

In case of the proton, the simulation can be checked with data from the liquid-hydrogen target measured with the same setup. For this purpose, the reactions $\gamma p \to p\eta \to p6\gamma$ and $\gamma p \to p\pi^0\pi^0 \to p4\gamma$ were analyzed using

similar procedures for invariant- and missing-mass analyses as discussed above. The proton detection efficiency $\epsilon_p(T, \Theta)$ is then simply given as the ratio of events with detected proton to all events of the respective reaction. The result, again averaged over the polar angles, agrees quite well with the simulation (see fig. 10, red dots). In case of the neutron, experimental information comes from the measurement of the neutron detection efficiency of the CB when it was installed at LEAR at CERN [69]. Therefore, in this case the simulation was done with the parameters (*e.g.* thresholds) characterizing the CB setup at CERN. The results are also compared in fig. 10. Agreement is quite good at larger T. Some discrepancies are visible at low T, however, here the result is strongly dependent on detector thresholds and neutron energy calibration, which may not have been reproduced perfectly in the present simulation of the old CB setup. In case of TAPS the neutron detection efficiency had been measured in an experiment at the Mainz MAMI accelerator using the $\gamma p \to n\pi^0\pi^+$ reaction for kinetic energies below 250 MeV [40]. The results are consistent with the simulation when the conditions of the Mainz setup are used (at 250 MeV simulated: $\epsilon_1 \approx 18.5\%$, from data: $\epsilon_1 \approx 19.1\%$).

Finally, it must be considered that neutrons from the $\gamma n \to n\eta$ reaction are identified in this experiment in events with seven neutral hits by first assigning six hits via the invariant mass analysis to the $\eta \to 3\pi^0 \to 6\gamma$ decay chain. This introduces efficiency losses due to combinatorial background. Therefore, a simulation was done, where events from $\gamma n \to n\eta$ were produced with a phase space event generator. The analysis then mimicked the whole reconstruction process, including the identification of the neutron out of the seven neutral hits. The resulting "effective" neutron detection efficiency is also shown in fig. 10 (blue squares). It is significantly lower than the "raw" neutron efficiency. The same kind of analysis was also done for the proton case. However, due to the additional information from Inner- and TAPS-veto detectors, in this case the effects are small. As final result of this analysis, recoil detection efficiencies for protons and neutrons are available as function of laboratory polar angle and kinetic energy.

The detection efficiency for η-mesons has been simulated as a function of their laboratory polar angles and kinetic energies in the same way as discussed in detail in [67]. The result is shown in fig. 11 (left-hand side) and compared to the distribution of the experimentally detected η-mesons (fig. 11, right-hand side). The branching ratio of the $\eta \to 6\gamma$ decay is not included in this efficiency (*i.e.* shown is the efficiency to detect η-mesons which decay with 100% branching ratio into six photons). The acceptance of the detector covers the full phase space of the reaction. However, the absolute values of the efficiency are small in particular for mesons at backward angles. This is due to the efficiency of the trigger, which was only based on photon detection in TAPS. Note that the recoil nucleon detection efficiencies discussed above do not include trigger efficiencies, since the meson is assumed to trigger.

The total detection efficiencies for the inclusive channel (no recoil nucleons required), the reactions in coincidence with recoil protons, and in coincidence with recoil neutrons were then calculated in two different ways to estimate systematic effects.

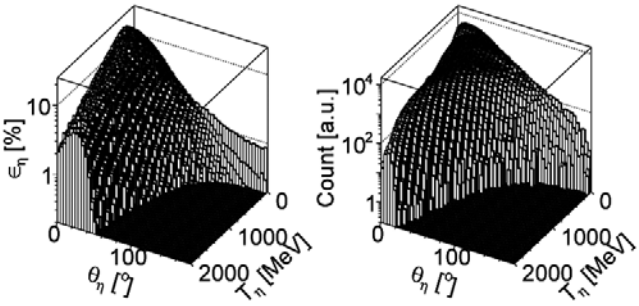

Fig. 11. Left-hand side: simulated detection efficiency (including trigger efficiency) for $\eta \to 6\gamma$ as a function of η laboratory kinetic energy and polar angle. Right-hand side: distribution of observed η-mesons in dependence on the same parameters.

In the first approach, η-photoproduction off quasi-free nucleons was simulated with a phase-space event generator, taking into account the effects of nuclear Fermi smearing. The simulated events were analyzed in the same way as the data and the detection efficiency ϵ_{ph} was calculated from the ratio of simulated and detected events as a function of incident photon energy and meson cm polar angle. The results are shown for some ranges of incident photon energy in fig. 12 as open squares. This simulation is in so far model dependent as the correlation between meson energies and angles as well as the correlation between mesons and recoil nucleons relies on the phase-space assumption. Possible deviations might occur in the three-body final state of meson, participant, and spectator nucleon for example due to final-state interactions.

In the second approach, the above-discussed distributions of the detection efficiencies for mesons and recoil nucleons as a function of particle laboratory angle and kinetic energy were applied event-by-event to the data. This step is completely model independent since the correction is only based on measured quantities (recoil nucleon energies from time-of-flight in TAPS and from reaction kinematics in CB). However, it does not correct for the missing-mass cuts (roughly a factor of two for the cut at $\Delta m < 0$ MeV). The loss factor due to this cut was again simulated with an event generator based on reaction phase space and corrected. The results for this almost model-independent efficiencies ϵ_{fac} from the quasi-factorization are shown as red dots in fig. 12. Obviously, the results obtained with both methods are in quite good agreement.

As expected, due to the trigger efficiency, for all reaction channels the detection efficiency is small at backward angles, in particular at higher incident photon energies. For the exclusive reactions, in particular the proton channel, it is also small for meson forward angles, corresponding to recoil nucleons emitted at large angles with small kinetic laboratory energies.

The angle-integrated detection efficiencies as a function of incident photon energy are shown in fig. 13. The curve for the proton channel shows some structure at

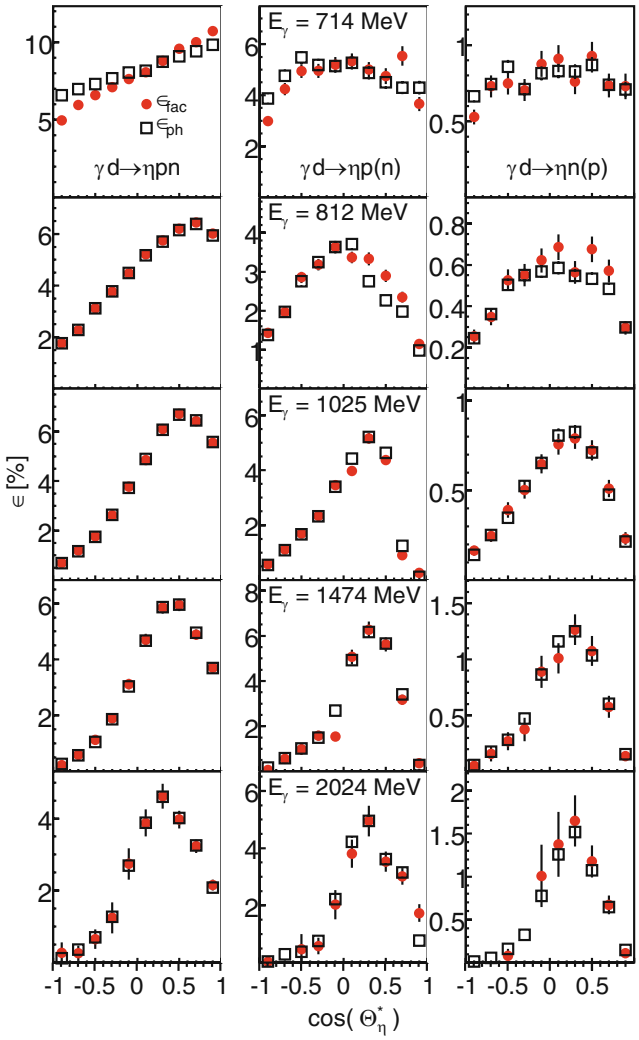

Fig. 12. Total detection efficiencies. Left column: $\gamma d \to \eta np$ (inclusive reaction), center column: $\gamma d \to \eta p(n)$ (recoil protons detected), right column $\gamma d \to \eta n(p)$ (recoil neutrons detected) for different incident photon energies as function of the η cm polar angle. (Red) dots: efficiency from quasi-factorization (ϵ_{fac}), (black) open squares: efficiency from phase-space simulation (ϵ_{ph}).

photon energies of 1 GeV. This can be explained with figs. 7, 10. At the lowest incident photon energies, all recoil protons are detected in TAPS. Around 900 MeV, part of the protons reaches the Barrel. Since the detection threshold in the Barrel is higher than in TAPS, this leads to a decrease of the efficiency. But since proton detection above the threshold was more efficient in the Barrel ($\approx$ 90%) than in TAPS ($\approx$ 60%) the overall efficiency rises again for higher incident photon energies. Since the neutron detection efficiency varies smoothly for both detectors no structure is present for quasi-free production off the neutron.

4.3.3 Summary of systematic uncertainties

Typical statistical uncertainties for the total cross-sections range from 0.5% to 5% for the inclusive data, from 1% to

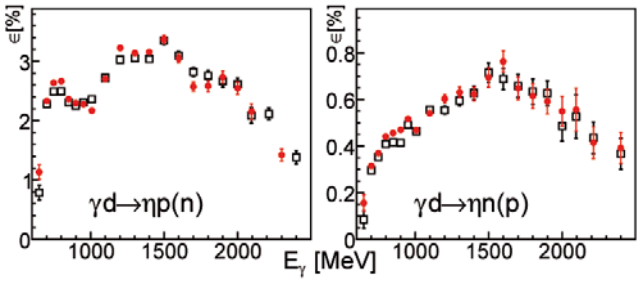

Fig. 13. Angle-integrated total detection efficiencies ϵ_{ph} (open squares) and ϵ_{fac} as a function of incident photon energy.

10% for the data with coincident protons and from 2% to 20% for the data with coincident neutrons (the first number corresponds to the range of the $S_{11}(1535)$ peak maximum, the second number to maximum incident photon energies). As discussed below, systematic uncertainties are of comparable size for high incident photon energies but dominate in the S_{11} range.

Systematic uncertainties are in three different categories: overall uncertainties which cancel exactly in the comparison of different reaction channels, uncertainties which are similar for different reaction channels and cancel to a large extent in ratios, and reaction channel related uncertainties which do not cancel.

In the first category all cross-sections are subject to an overall systematic uncertainty of the photon flux of $\approx$ 10%. The overall uncertainty of the target thickness of a few per cent is comparably small and the uncertainty of the decay branching ratio (below 1%) is negligible.

The second class of uncertainties is related to the detection of the η-mesons. The main steps of the analysis, which have to be reproduced by the Monte Carlo simulations, are the detection, identification, and calibration of photon showers, the invariant-mass analysis for the identification of the mesons, and the missing-mass analysis removing background from reactions with additional mesons in the final state.

At the most basic level, a stringent limit for systematic uncertainties arising from the detection of photons and the subsequent identification of mesons via the invariant-mass analysis can be derived from a comparison of the results for η-photoproduction off the free proton. This has been previously analyzed for the same setup for the $\eta \to 2\gamma$ and the $\eta \to 6\gamma$ decay channels [23,26,29]. Systematic effects would enter cubed into the six-photon channel, but agreement was found on average at the 2% level. Furthermore, also the present simulations with the two different methods —one relying on the phase-space event generator, the other using the quasi-factorization of the detection efficiency— are in good agreement. From this we estimate a typical 5% uncertainty for a successful η-reconstruction. The uncertainty related to the separation of signal and background in the invariant mass spectra (fitted with line shape and background polynomial) is not explicitly treated as an additional systematic effect, but the fit uncertainty is included into the statistical errors.

Table 2. Summary of systematic uncertainties for the quasi-free reactions.

Source	$\gamma d \to (n)p\eta$	$\gamma d \to (p)n\eta$
Overall normalization[a)]	10%	10%
η detection[b)]	8%–20%	8%–20%
Recoil nucleon detection	8%	15%

a) Photon flux, target thickness, decay branching ratios.
b) Trigger efficiency, η analysis cuts, η detection efficiency. The first number corresponds to the threshold energy range, the second to $E_\gamma = 2.5\,\mathrm{GeV}$, and linear interpolation is used in between.

Finally, the missing mass cut deserves special attention (see fig. 6). At incident photon energies below 0.8 GeV, the spectra are practically background free. At higher energies background from $\eta\pi$ final states and the tail of the missing mass distribution for single η-production arising from the momentum distribution of the bound nucleons mix. The simulations indicate that the background reactions do not contribute in the region of negative missing masses (cf. fig. 6). Since only those events were accepted, background contamination is estimated at most at the per cent level. However, due to this cut, the simulation must closely reproduce the shape of the missing mass peak, including effects of Fermi motion. This is the case for the background free peaks at low incident photon energies and for all energies for the peak shape at the non-contaminated side. In the background contaminated regions the data can be reproduced by a summation of the simulated structures for peak and background (with properly adjusted relative contributions), but no direct check is possible. From the agreement between data and simulations and the fraction of the missing mass signal extending into the tail region we estimate for the missing-mass analysis a systematic uncertainty of 3% for the total cross-section in the threshold region rising to 15% at 2.5 GeV. Altogether, independently of the reaction channel we estimate the systematic uncertainty for the η detection at 8% at production threshold rising to 20% at 2.5 GeV.

The most critical uncertainties are related to the detection of the recoil nucleons. From the agreement between simulated and measured efficiencies we estimate on average $\approx 8\%$ uncertainty for recoil protons and 15% for recoil neutrons. Uncertainties can be larger (in particular for the proton) for kinematical parameters where they are partly detected in TAPS and partly in the CB, *i.e.* for incident photon energies from 0.8 GeV to 0.9 GeV and $\cos(\Theta^\star_\eta) > 0$ and at higher incident photon energies for $\cos(\Theta^\star_\eta) \approx -0.1$ (cf. fig. 7). The above discussed systematic uncertainties are summarized in table 2.

As already discussed in [14,15] the nucleon detection uncertainty may be checked in an independent way. The cross-section of the coherent process $\gamma d \to d\eta$ is negligible [42] compared to the quasi-free reaction. Therefore, the quasi-free reactions σ_{np} (inclusive, no condition for recoil nucleons), σ_p (coincident recoil protons), and σ_n (coincident recoil neutrons) must obey $\sigma_{np} = \sigma_p + \sigma_n$. This is demonstrated in fig. 14, where the sum of the

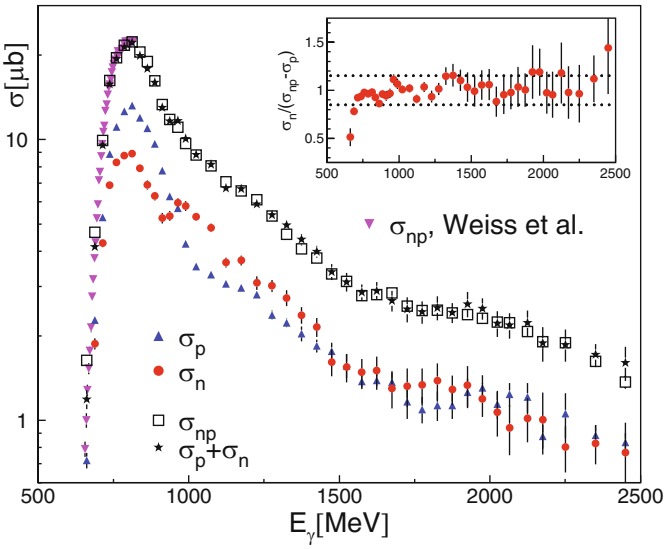

Fig. 14. Comparison of total cross-sections. (Blue) upward triangles: quasi-free proton cross-section σ_p, (red) dots: quasi-free neutron cross-section σ_n, (black) open squares: inclusive quasi-free cross-section σ_{np}, (black) stars: $\sigma_n + \sigma_p$. Downward (magenta) triangles: inclusive quasi-free cross-section from Weiss *et al.* [41]. Insert: ratio of neutron cross-sections.

quasi-free proton and neutron cross-sections is compared to the inclusive cross-section. The agreement is excellent and allows an independent extraction of the neutron cross-section as $\sigma'_n = \sigma_{np} - \sigma_p$. The ratio σ_n/σ'_n of the two results is shown in the insert of fig. 14. The agreement is within statistical uncertainties for most data points and typical deviations do not exceed the 15% level. As a further test, the distribution of the deviations $\delta\sigma_i$ normalized by the statistical uncertainties $\Delta\sigma_i$

$$\frac{\delta\sigma_i}{\Delta\sigma_i} \equiv \frac{\mathrm{d}\sigma'_n/\mathrm{d}\Omega - \mathrm{d}\sigma_n/\mathrm{d}\Omega}{\sqrt{\Delta^2(\mathrm{d}\sigma'_n/\mathrm{d}\Omega) + \Delta^2(\mathrm{d}\sigma_n/\mathrm{d}\Omega)}} \qquad (9)$$

for all data points (420 entries) of the angular distributions from production threshold to 2.5 GeV is compared to a Gaussian distribution in fig. 15. The fitted Gaussian distribution corresponds to a width of $\sigma = (1.25 \pm 0.10)$ and a mean of $\mu = (0.034 \pm 0.110)$, fairly close to a standard Gaussian distribution. In particular, the mean is not significantly different from zero so that no indication for a systematic deviation is indicated.

This is a very stringent test for systematic uncertainties related to the recoil nucleon detection since it is the neutron detection efficiency which enters in the extraction of σ_n, while only the inherently different proton detection efficiency enters into σ'_n. The result means that the corresponding systematic uncertainties quoted in table 2 derived from the analysis of the recoil nucleon detection efficiencies are probably pessimistic.

Due to this good agreement total neutron cross-sections as function of incident photon energy are given in this paper as weighted averages $\langle\sigma_n\rangle$ of σ_n and σ'_n which improves the statistical quality. For the shape of the angular distributions only the direct measurement with

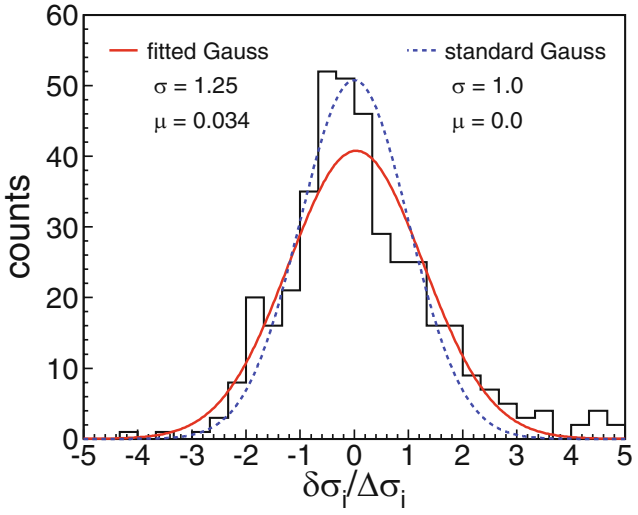

Fig. 15. Distribution of deviations between $d\sigma_n/d\Omega$ and $d\sigma'_n/d\Omega = d\sigma_{np}/d\Omega - d\sigma_p/d\Omega$. Solid (red) curve: fitted Gaussian distribution (width $\sigma = 1.25$, mean $\mu = 0.034$), dashed (blue) curve: standard Gauss: ($\sigma = 1$, $\mu = 0$).

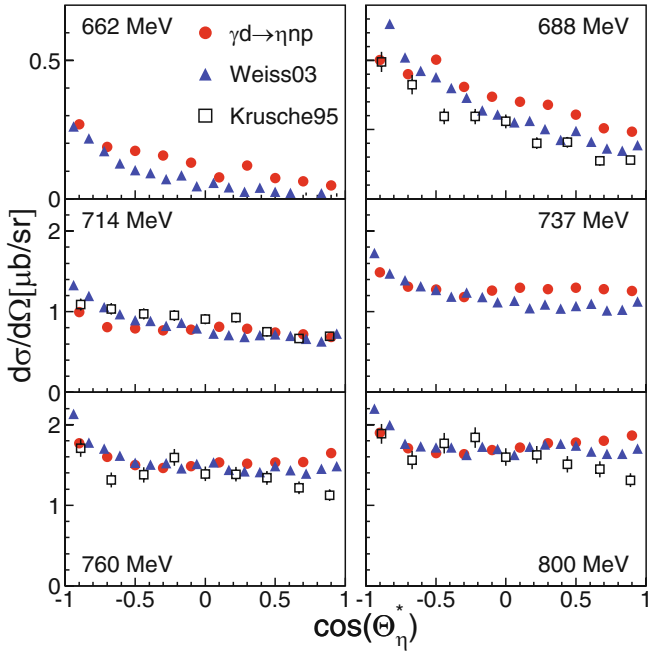

Fig. 16. Comparison of the inclusive cross-section σ_{np} to previous results (Krusche95 [38], Weiss03 [41]). Errors are only statistical.

the neutron coincidence is used since due to the small detection efficiency at extreme angles (in particular for the proton) systematic effects for σ'_n are larger.

5 Results and discussion

Throughout this paper all quasi-free differential cross-sections are given in the cm (center-of-momentum) system of the incident photon and a target nucleon *at rest*. This simplifies the comparison to angular distributions measured off the free nucleon since apart from the immediate threshold region such quasi-free cross-sections are only moderately smeared out by Fermi motion in this system, while in the γd system they have completely different shapes due to the Lorentz boosts (see [38] for details).

5.1 Comparison to previous results

The inclusive cross-section σ_{np} has been previously measured twice [38,41] at the Mainz MAMI accelerator with different configurations of the TAPS detector (the setup used for [41] covered a larger solid angle than for [38]) up to incident photon energies of 0.8 GeV. The total cross-section from [41] is included in fig. 14. Typical angular distributions are compared in fig. 16.

The shapes of the angular distributions are similar for all three experiments. There is a systematic deviation between the two previous measurements with the present data for the absolute scale of the two lowest-energy bins. These are, however, probably not due to the normalization of the cross-section data but to the systematic uncertainty in the measurement of the incident-photon energy. Both bins are located in the extremely sharp rise of the cross-section close to threshold (cf. fig. 14). In this range, already small effects in the determination of the incident photon beam energy are strongly amplified in the magnitude of the cross-section. The resolution for the incident-photon energy in the threshold region was better for the previous MAMI experiments, which aimed at very precise threshold measurements in view of FSI effects. The MAMI data had typically 2 MeV bin width for the incident photon energy with an absolute calibration uncertainty of less than 1 MeV while the present data were measured with 10 MeV bin width and a calibration uncertainty of several MeV. Therefore, the systematic quality of the previous data in the immediate threshold region is almost certainly superior. However, this region is not of much interest for the present experiment. Agreement is much better and within systematic uncertainties at higher incident photon energies. In this range, the data from [38] have somewhat larger systematic uncertainties than the other two data sets due to the restricted solid-angle coverage.

The quasi-free proton data are compared in figs. 17, 18 to free proton data. The total cross-section for the quasi-free reaction has been corrected for the effects of Fermi motion in the following way. The well-known energy dependence of the cross-section for η-production off the free proton was folded with the momentum distribution of the bound proton using the deuteron wave function in momentum space from [70] as described in [38]. The ratios of free and folded cross-section (solid line in the insert of fig. 17) were then applied as correction factors to the measured quasi-free cross-section. Measured and corrected quasi-free cross-sections are compared in the insert of fig. 17. The corrected quasi-free cross-section is then compared in fig. 17 to the data base of free proton results. The agree-

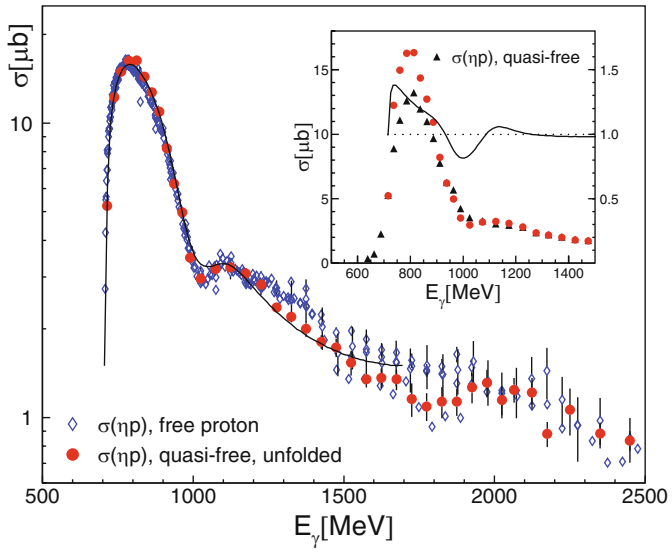

Fig. 17. Comparison of the total cross-section of quasi-free production off the bound proton to free proton data. Filled (red) circles: quasi-free σ_p corrected for effects of Fermi motion (see text). Open (blue) diamonds: free proton data from [16, 21–23, 29, 30, 32]. Total cross-sections for the free proton data from [22, 30] have been estimated from the published differential cross-sections. Solid line: eta-Maid model [35]. Insert: comparison of quasi-free proton data (black triangles) to quasi-free proton data after correction of Fermi motion effects (red filled circles) (see text). Solid curve: ratio of free and folded cross-section (scale at right-hand side).

ment between the free and quasi-free data is excellent for most incident photon energies. This indicates that no nuclear effects (FSI, re-scattering) except nuclear Fermi motion influence the quasi-free data. The latter effects are significant in the steep slopes of the cross-section for photon energies below 1.1 GeV, they are negligible in the flat region at higher incident photon energies.

Angular distributions for the free and quasi-free $\gamma p \to p\eta$ reactions are summarized in fig. 18. The quasi-free data have not been corrected for Fermi motion. They have been fitted with Legendre polynomials

$$\frac{\mathrm{d}\sigma}{\mathrm{d}\Omega} = \frac{q_\eta^\star}{k_\gamma^\star} \sum_{i=0}^{3} A_i P_i(\cos(\Theta_\eta^\star)), \qquad (10)$$

where the A_i are expansion coefficients (higher-order coefficients were not significant). The phase-space factor $q_\eta^\star/k_\gamma^\star$ ($q_\eta^\star$, $k_\gamma^\star$: meson and photon cm momenta) is evaluated for the photon–nucleon-at-rest cm system.

At incident photon energies above 1.1 GeV the angular distributions are in excellent agreement with the quasi-free data. Close to threshold the large influence of Fermi motion is visible, but the comparison of the quasi-free data to the MAID model result folded with Fermi motion (dashed lines) demonstrates that this effect is well under control. A large deviation between free and quasi-free data occurs also for incident photon energies around 975 MeV. In this region the pronounced "dip" in the total free cross-section is filled in by Fermi motion from the tail of the S_{11} resonance, however again the folded cross-section is in good agreement with experiment.

In summary, we conclude that after correction for the effects of nuclear Fermi motion the absolute scale and the shape of the angular distributions of the quasi-free proton data agree very well with the most recent and most precise measurements of η-photoproduction from the free proton. This is the systematic basis for the discussion of the quasi-free neutron data.

5.2 The quasi-free reaction $\gamma n \to n\eta$ off the neutron

The total cross-section of the quasi-free reaction off the neutron is compared to the quasi-free proton data in fig. 19, which also shows the neutron/proton cross-section ratio. The behavior at low incident photon energies ($E_\gamma \leq 800$ MeV) is consistent with previous results. The cross-section ratio in the S_{11} region is close to 2/3 and rises to the kinematic threshold close to unity because in the immediate vicinity of the threshold the participant-spectator approach becomes meaningless (dictated by energy and momentum conservation at threshold "participant" and "spectator" nucleon have always identical momenta).

Around incident photon energies of 1 GeV, corresponding to $W \approx 1.7$ GeV a bump-like structure is visible in the neutron cross-section, which is not seen for the proton. In fact, it is even more pronounced in the ratio of neutron and proton data, which shows a sharp rise around $E_\gamma = 1$ GeV. Before we discuss this structure in detail, we compare the angular distributions of the two reactions, which are summarized in fig. 20. They have been fitted with the Legendre series from eq. (10) and the coefficients are shown in fig. 21.

The coefficients of the quasi-free proton data are in good agreement with the free proton data as expected from fig. 18. The largest deviations occur for a few values of the A_3 coefficient close to the threshold, this might be due to uncorrected Fermi motion effects.

The neutron results obtained from the analysis with coincident recoil neutrons (σ_n) and from the difference of inclusive data and data with coincident protons $\sigma_n' = \sigma_{np} - \sigma_p$ (filled and open circles in fig. 20) are also in good overall agreement, some discrepancies occur for the extreme angles, in particular in forward direction. Here, one should note that the detection efficiency for the reaction with coincident recoil protons almost vanishes for the extreme forward angles of the η-meson (see fig. 12), so that σ_n' is less well defined in this regime.

For the comparison of proton and neutron cross-sections we discuss three different energy ranges. At high incident photon energies above 1.5 GeV, the absolute magnitude of the cross-sections as well as the strongly forward peaked shape of the angular distributions are almost identical. This is the energy region, were previous model analyses of free proton data (see, *e.g.*, [23]) have identified dominant contributions from t-channel background terms. These contributions seem to be similar for protons and neutrons, which is not unexpected when considering

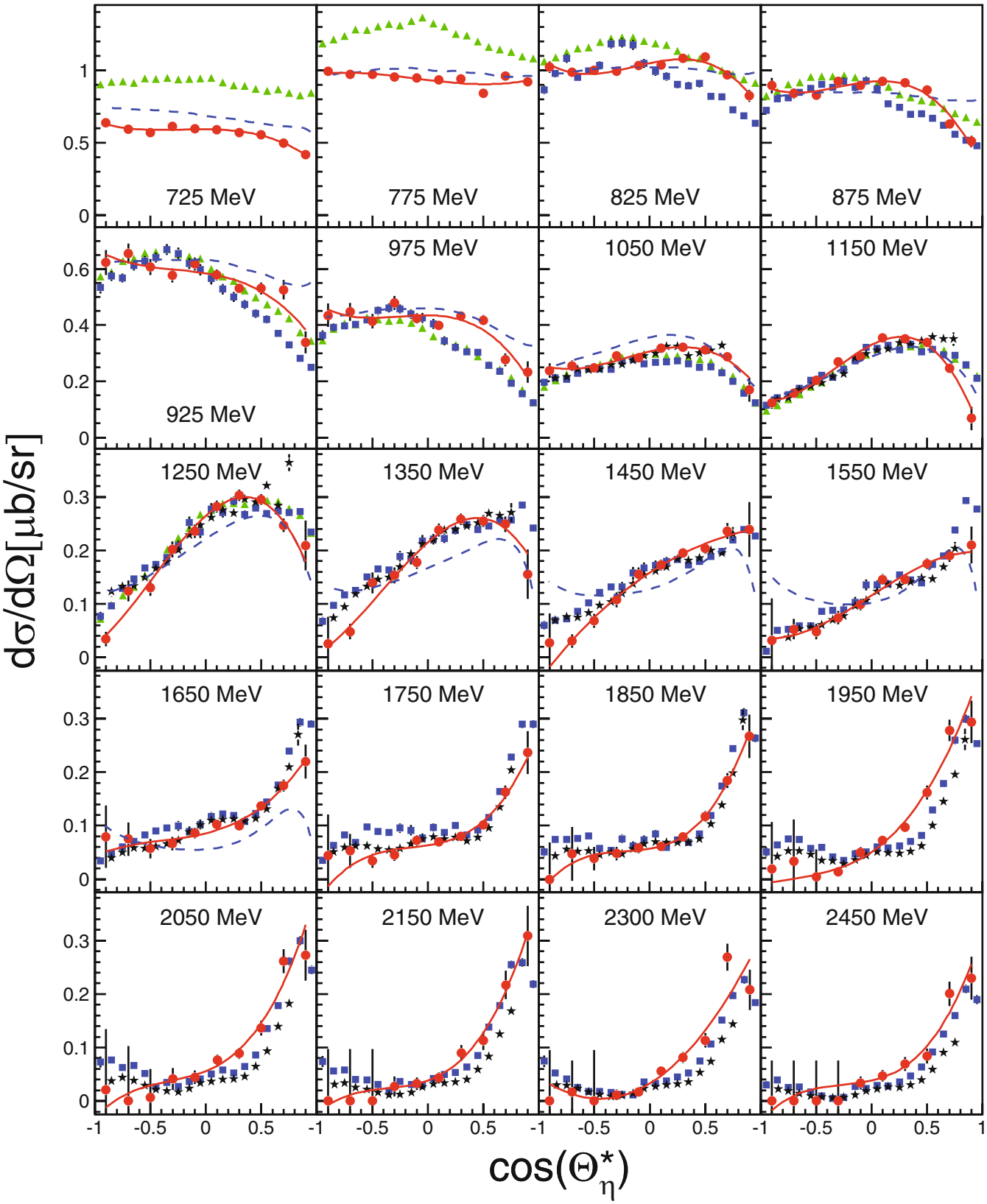

Fig. 18. Differential cross-sections for $\gamma p \to p\eta$. (Red) filled circles: quasi-free data from present experiment (not corrected for Fermi motion), (Red) solid lines: fits with Legendre polynomials. Other symbols free proton data: (blue) squares: [29], (black) stars: [30], (green) triangles: [32] (data have been partly re-binned to cover the same energy ranges). Dashed (blue) lines: Eta-Maid model [35] folded with Fermi motion

isospin invariance. Agreement with the MAID model at higher incident photon energies is not good, the observed forward peaking of the cross-section is not reproduced. The analysis of the previous ELSA proton data [23,26,29] in the framework of the Bonn-Gatchina model had found a strong contribution of a $D_{15}(2070)$ state to η-production at large incident photon energies. This state is not visible as a bump in the total cross-section, not even like the small indication of the P resonances at $W \approx 1.7\,\mathrm{GeV}$. It was extracted from the analysis of the angular distributions. The present neutron/proton ratio of the total cross-section might show some structure in this energy region (cf. fig. 19, bottom part), however at the very limit of statistical significance.

The total cross-section for quasi-free η-production off the proton and the neutron are quite different at low incident photon energies (below 900 MeV) in the range of the second resonance region. In this regime, the absolute magnitudes of the cross-sections reflect the ratio of the helicity amplitudes of the $S_{11}(1535)$ resonance (see eqs. (1), (2)). The shape of the angular distributions is dominated by the interference between the $S_{11}(1535)$ and the $D_{13}(1520)$ resonances, which involves a term proportional to the A_2 coefficient of the Legendre series. The electromagnetic helicity-1/2 couplings $A_{1/2}$ of the D_{13} have identical signs for proton and neutron, while the S_{11} couplings have different signs. Therefore, the interference term changes sign from proton to neutron, giving rise to negative A_2 coefficients for the proton and positive ones for the neutron [41]. This effect is also reflected in the model calculations [35,51,52].

In the most interesting range around 1 GeV incident photon energy, where the peak-like structure appears in the total neutron cross-section, proton and neutron angular distributions are not very different (apart from the absolute scale). In this region, the S_{11}-D_{13} interference is not visible any more (A_2 for proton and neutron is small and negative) and the A_1 coefficient shows a zero crossing with very steep rise. It was already discussed in [28] that the simplest explanation for a rapidly varying A_1 coefficient is an interference between S and P waves. This explanation seems to be natural since it is well known that in this energy region the tail of the $S_{11}(1535)$ resonance, the $S_{11}(1650)$ resonance, and the $P_{11}(1710)$ and/or $P_{13}(1730)$ resonances contribute. The model analyses still disagree in the relative importance of the two P-wave states. The η-MAID model [35] finds a dominant contribution from the P_{11}, while the Bonn-Gatchina analysis [37] prefers the P_{13} state. Very preliminary results from a measurement of the $\vec{\gamma}\vec{p} \to p\eta$ reaction (circularly polarized beam, longitudinally polarized target) at ELSA [71] indicate a dominant helicity-1/2 component in this energy region, which is more in line with the MAID analysis favoring the P_{11} contribution. If one assumes only S_{11} and P_{11} states (E_{0+} and M_{1-} multipoles), the A_1 coefficient would simply be proportional to $\mathrm{Re}(E^{\star}_{0+} M_{1-})$ and thus the fast zero crossing would imply a rapid phase change between these multipoles indicating, that one is going through resonance around 1 GeV.

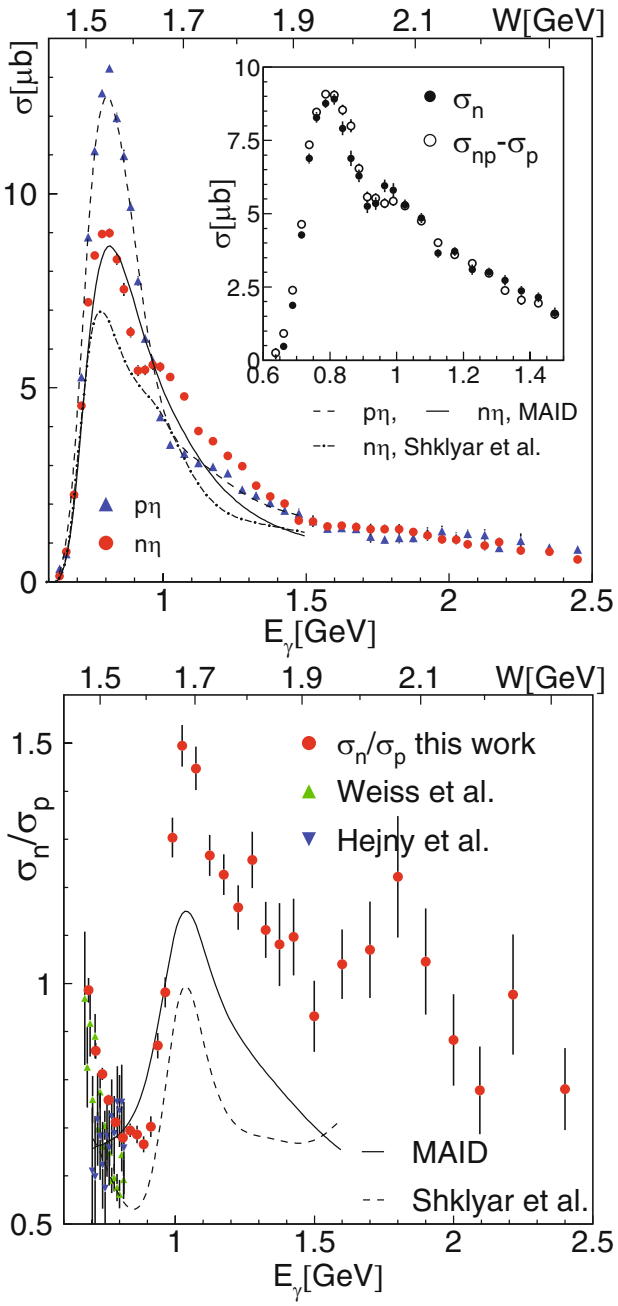

Fig. 19. Comparison of quasi-free proton and neutron excitation function. Upper part: Curves model results, dashed: Eta-MAID for proton [35], solid: Eta-MAID for neutron [35], dash-dotted: Shklyar *et al.* [51]. Insert: comparison of the total neutron cross-sections extracted from the coincident measurement of neutrons (σ_n) and the difference of inclusive and proton data (σ'_n). Bottom part: Cross-section ratio σ_n/σ_p compared to previous data from quasi-free production off the deuteron [41] and off ^{4}He [40] and model results (solid: MAID [35], dashed: Shklyar *et al.* [51]) folded with Fermi motion.

It is, however, not yet understood, whether the structure observed in the total neutron cross-section at the same incident photon energy is somehow related to contributions from these resonances. Structures in the total

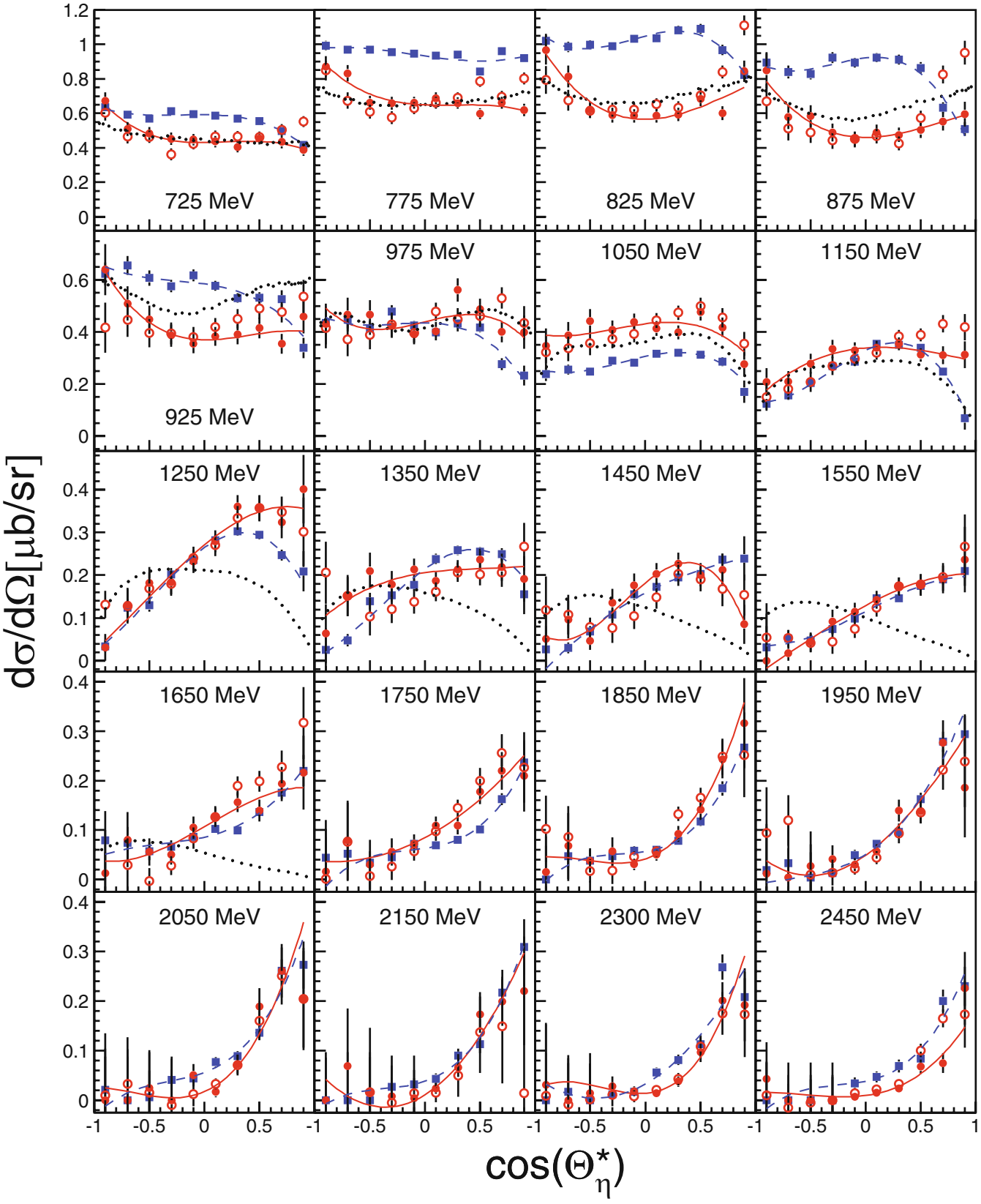

Fig. 20. Quasi-free angular distributions, labels indicate incident photon energy. (Blue) squares: proton coincidence σ_p, (red) filled circles: neutron coincidence σ_n, (red) open circles: difference of inclusive and proton σ'_n. Dashed (blue) curves: fit of proton data, solid (red) curves: fit of neutron data, dotted (black) curves: Eta-MAID for neutron folded with Fermi motion.

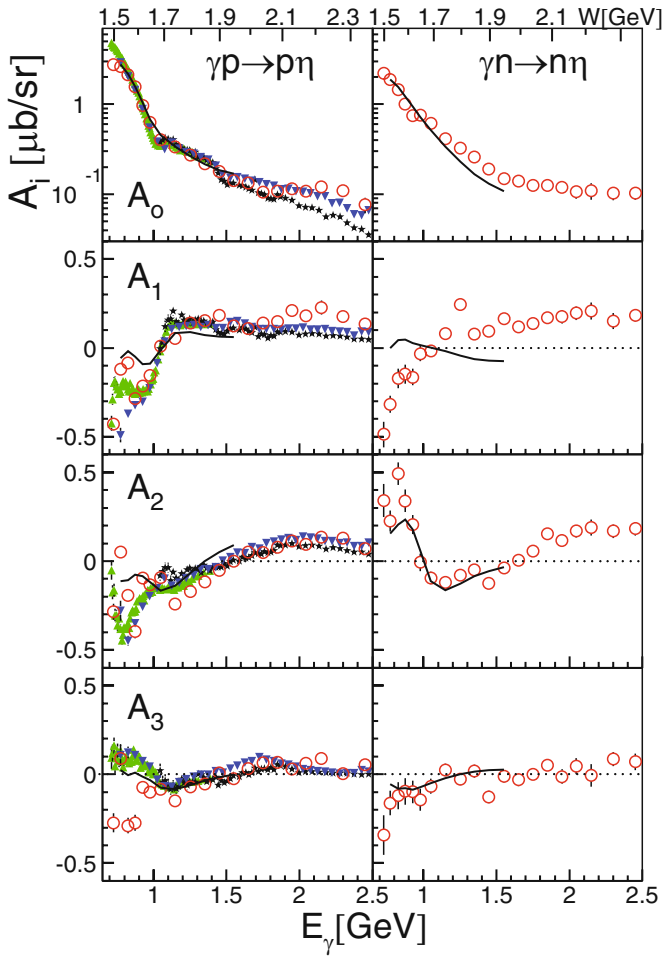

Fig. 21. Coefficients of the Legendre series of the fits in figs. 18, 20, Left-hand side: quasi-free proton. Open (red) circles: present quasi-free data, (blue) downward triangles: Bonn ELSA data [29], (black) stars: CLAS data [30], (green) upward triangles: Mainz MAMI data [32]. Right-hand side: quasi-free neutron (from neutron coincidence σ_n). Open (red) circles: present quasi-free data, solid lines: Eta-MAID [35]. Note the logarithmic scale for A_0.

cross-section can obviously not arise from interferences between different partial waves. Therefore, different scenarios involving contributions from specific resonances as well as interference patterns in the same partial wave have been discussed in the literature. Fix, Tiator, and Polyakov [54] have investigated whether the data could be consistent with the excitation of a narrow P_{11}-state. This work was motivated by the idea that the P_{11}-state of the proposed anti-decuplet of pentaquark states should be relatively narrow (width on the order of 10 MeV), have a strong electromagnetic coupling to the neutron, and a large ηN decay branching ratio [46,47]. They used two different versions of the η-MAID model, the standard version [35] and the reggeized version [72] as basis of their fits. The standard version, including a large contribution from the $D_{15}(1675)$ resonance, reproduces fairly well the experimental ratio of neutron and proton cross-sections, although it does not show the structure observed in the neutron data around photon energies of 900 MeV (see also discussion in the next section). The reggeized version with a much smaller contribution of the D_{15} reproduces the data only when an additional narrow resonance is introduced (taken as P_{11}). Since the data are smeared out by Fermi motion, the width of this additional state is uncertain and could be as narrow as 10 MeV (roughly 40 MeV as upper limit) [54]. Similarly, an analysis performed in the framework of the Bonn-Gatchina model (BoGa) [55] can reproduce the neutron data reasonably well with three completely different scenarios, by either adding a "conventionally" broad P_{11} resonance, a very narrow P_{11} state, or even by a careful adjustment of the interference pattern for the S-wave amplitudes. Shklyar, Lenske, and Mosel [51] find solutions in the framework of the Giessen coupled channel model with bump-like structures in the neutron excitation function around $E_\gamma \approx 1$ GeV just from coupled channel effects in the S_{11}-P_{11} sector, without introducing any additional resonance. A similar result from a coupled-channels K-matrix approach was presented by Shyam and Scholten [52] who report a bump-like structure arising from superpositions and interferences of contributions from the $S_{11}(1535)$, $S_{11}(1650)$, $P_{11}(1710)$, and $P_{13}(1720)$ states. However, this structure appears broader than our experimental results discussed below. Finally, Döring and Nakayama [53], using an S-wave coupled channel model, find a "dip-bump" structure in the neutron cross-section related to the opening strangeness thresholds of $K\Lambda$ and $K\Sigma$ photoproduction around 900 MeV and 1050 MeV. Such unitary cusps are for example well-known for pion production reactions. The cusp structure in π^0 and π^+ photoproduction off the proton at the η-production threshold was discussed in detail in [73], and the cusp structure in $\gamma p \to p\pi^0$ at the $\gamma p \to n\pi^+$ threshold was analyzed in [74].

From the experimental side obviously two pieces of information are missing to distinguish between these different scenarios. In the absence of any results for polarization observables, it is impossible to isolate the responsible partial wave(s). Measurements of polarization observables like the helicity asymmetry E (longitudinally polarized target, circularly polarized beam), the target asymmetry T (transversely polarized target), and the asymmetry F (transversely polarized target, circularly polarized beam) have been initiated at the Bonn and Mainz accelerators, for η photoproduction off the free proton also at the CLAS experiment at Jlab. Furthermore, the influence of the momentum distribution of the bound neutron obscures the intrinsic shape of the bump structure for the free neutron. To overcome this difficulty, we present in the following section a new analysis of the present data, based not on the incident photon energy but on the invariant mass of the η-N final state, which is not affected by Fermi motion.

5.3 The η-nucleon invariant mass distributions

In the previous sections we discussed the cross-sections as a function of the incident photon energy measured with

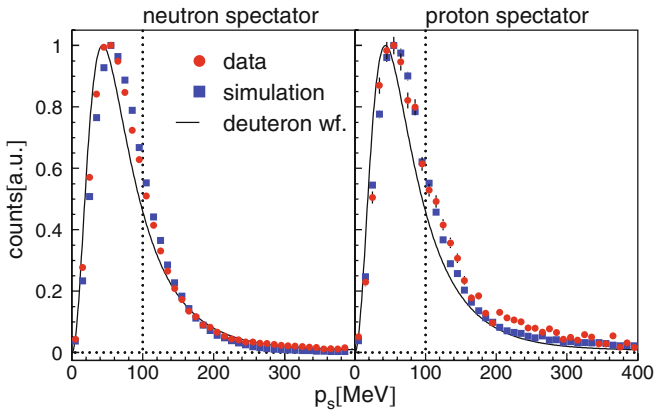

Fig. 22. Momentum distributions of spectator nucleons. (Red) dots: reconstructed from data, (black) lines: expected from deuteron wave function [70], (blue) squares: Monte Carlo simulation including detector response. Left-hand side: neutron spectator (*i.e.* recoil proton detected), right-hand side: proton spectator (*i.e.* recoil neutron detected).

the tagging spectrometer. Due to the momentum distribution of the bound nucleons, each value of incident photon energy corresponds to a broad distribution of invariant masses W of the η–participant-nucleon pairs, giving rise to the Fermi smearing of all narrow structures. However, in principle we can directly extract W from the four-momenta of the η and the participant nucleon. We have already shown in [14] that the bump around 1.7 GeV in W becomes then much narrower. In that analysis only data with η-mesons emitted at backward angles were included, since then the kinetic energy of the neutron detected in the TAPS detector can be determined from a time-of-flight measurement. However, this analysis can be extended to the full data set, using the kinematical overdetermination of the data.

All kinematic variables (incident photon beam energy, target deuteron at rest) of the initial state are known. For the final state the four-momentum of the η-meson, the mass of participant and spectator nucleon and the recoil direction of the participant nucleon (polar angle Θ and azimuthal angle Φ) are known. Missing is only the three-momentum of the spectator and the kinetic energy of the participant nucleon. But these four variables can be extracted using energy and momentum conservation which provide four equations. Monte Carlo simulations using the GEANT package have shown that with this reconstruction a typical experimental resolution of FWHM ≈ 25 MeV for W is achieved.

As result of such an analysis fig. 22 shows the distribution of the momenta of the spectator nucleons, constructed event-by-event from the reaction kinematics. In plane-wave approximation with negligible FSI effects, these momenta must reflect the momentum distribution of the bound nucleons. As demonstrated in the figure, this is quite well fulfilled. Data generated with a participant-spectator Monte Carlo simulation using the deuteron wave function as input and including the response of the detector reproduce the measured distributions. For further analysis one can in principle cut away events with large spectator momenta, which are not close to quasi-free kinematics. However, as it turned out (see figs. 23, 24), such a cut has not much impact (in particular it has not on the angular distributions) apart from reducing counting statistics, so that it was not used for the differential cross-sections.

For the absolute normalization of the total cross-section as function of W, the photon flux $\mathrm{d}N_\gamma/\mathrm{d}E_\gamma$ measured as a function of incident photon energy E_γ, was folded with the nucleon momentum distribution to obtain the flux $\mathrm{d}N_\gamma/\mathrm{d}W$ in dependence of the final-state invariant mass. The results for the total quasi-free cross-sections of the proton and the neutron with and without cut on spectator momentum are summarized in figs. 23, 24. For both analyses good agreement between the quasi-free proton data and the world data set of free proton data is found. The neutron data show a pronounced, narrow peak around $W \approx 1.7$ GeV. The position of this peak coincides with a dip in the proton excitation function.

In the following we discuss in more detail first the range of the $S_{11}(1535)$ resonance and then the narrow structure in the neutron excitation function.

5.3.1 The region of the $S_{11}(1535)$ resonance peak

The region of the $S_{11}(1535)$ is interesting for two reasons. First since this is a well-studied state, it can serve as a test case for the extraction of resonance parameters from quasi-free data with the above-discussed kinematical reconstruction. Furthermore, the results contribute to the discussion up to which energy range the observed cross-section for η-photoproduction is dominated by the $S_{11}(1535)$.

In the region of the $S_{11}(1535)$ peak all data have been fitted with a parameterization of this resonance as Breit-Wigner curve with energy-dependent width [12]:

$$\sigma(W) = \frac{q^\star_\eta}{k^\star} \cdot \frac{k^\star_R}{q^\star_{\eta R}} \cdot \frac{2m_N \cdot W_R \cdot b_\eta \cdot (A^N_{1/2})^2 \cdot \Gamma_R}{(W^2_R - W^2)^2 + W^2_R \Gamma^2_R x^2} \qquad (11)$$

with

$$x = b_\eta \cdot \frac{q^\star_\eta}{q^\star_{\eta R}} + b_\pi \cdot \frac{q^\star_\pi}{q^\star_{\pi R}} + b_{\pi\pi}, \qquad (12)$$

where W_R, Γ_R are resonance position and width, $k^\star_R$, $q^\star_{\eta R}$, $q^\star_{\pi R}$ are incident photon momentum, η-momentum and π-momentum at resonance position in the photon–nucleon-at-rest cm frame, $A^N_{1/2}$ is the electromagnetic helicity-1/2 coupling, $b_\eta = 0.5$, $b_\pi = 0.4$, and $b_{\pi\pi} = 0.1$ have been used as branching ratios for the $N\eta$, $N\pi$, and $N\pi\pi$ decays of the resonance, and m_N is the nucleon mass.

The data have been fitted up to $W \approx 1.6$ GeV, where the proton and neutron cross-sections start to deviate and obviously the line-shape can no longer be dominated by the S_{11} resonance. The fit results are shown in fig. 23 and the parameters are summarized in the upper part of table 3. The results demonstrate the following. Breit-Wigner

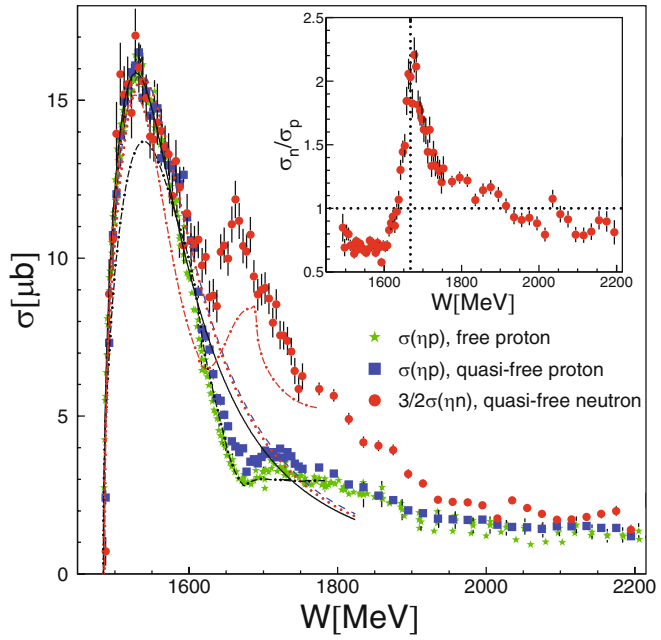

Fig. 23. Total cross-sections as a function of final-state invariant mass W without cut on spectator momentum. (Red) dots: quasi-free neutron, (blue) squares: quasi-free proton, (green) stars: free proton data. Curves: fitted (up to W = 1600 MeV) $S_{11}(1535)$ line shapes. (Black) solid: free proton, (blue) dashed: quasi-free proton, (red) dotted: quasi-free neutron. Dash-dotted curves: model results from [53]. Insert: ratio of quasi-free neutron–proton data.

Table 3. Result of Breit-Wigner fits. $N\eta$ branching ratio of S_{11} is assumed as b_η=0.5. Upper part of table: Comparison of fits of $S_{11}(1535)$ resonance for free proton, quasi-free proton, and quasi-free neutron data to PDG estimates [36] and BoGa model fit [55]. Bottom part: fit of neutron data with S_{11}. resonance and two further Breit-Wigner curves. All uncertainties of fit parameters are statistical only.

$S_{11}(1535)$	$W^{(a)}$ [MeV]	$\Gamma^{(a)}$ [MeV]	$A^{(b)}_{1/2}$ $[10^{-3}\,\mathrm{GeV}^{-1/2}]$
PDG	1535 ± 10	150 ± 25	$A^p_{1/2}$: 90 ± 30
	(1510 ± 10)	(170 ± 80)	$A^n_{1/2}$: 46 ± 27
BoGa[(c)]	–	–	$A^p_{1/2}$: 90 ± 25
	(1505 ± 20)	(145 ± 25)	$A^n_{1/2}$: 80 ± 20
$\gamma p \to p\eta$	1536 ± 1	170 ± 2	106 ± 1
$\gamma d \to (n)p\eta$	1544 ± 2	181 ± 13	109 ± 3
$\gamma d \to (p)n\eta$	1546 ± 3	176 ± 20	90 ± 4
$\gamma d \to (p)n\eta$			
$S_{11}(1535)$	1535 ± 4	166 ± 23	88 ± 6
"broad BW"	1701 ± 15	180 ± 35	–
"narrow BW"	1663 ± 3	25 ± 12	–

(a) Breit-Wigner mass, in brackets pole position.
(b) Only magnitudes, no signs.
(c) Only pole positions given, no Breit-Wigner mass.

mass and width of the resonance extracted from the quasi-free proton and neutron data are in excellent agreement. The agreement with the free proton data is good, but not within statistical uncertainties. This had to be expected due to the finite W resolution of the quasi-free data, which tends to increase the width and to shift the resonance position slightly upward. These parameters are also in good agreement with the values given by the particle data group [36] and the Bonn-Gatchina analysis [55] of the present data. Note that for the BoGa analysis not Breit-Wigner masses but pole positions are given, which agree with the PDG parameters. The almost perfect agreement of the shape of the S_{11}-peaks for the proton and neutron data in this range is also further evidence that this shape is alone dominated by the $S_{11}(1535)$. Effects *e.g.* from the destructive interference of the two S_{11} resonances, which are important at higher incident photon energies, should be different for proton and neutron since the ratios of the electromagnetic couplings of these two resonances are quite different for protons and neutrons.

The electromagnetic helicity couplings $A^N_{1/2}$ found from the fits agree for free and quasi-free proton data. The proton couplings are slightly higher than the PDG value and the BoGa result. This could be a systematic effect, since all non-$S_{11}(1535)$ contributions are neglected in the fit. The only large discrepancy arises for the neutron helicity coupling between the present and BoGa results, on the one hand and the PDG value, on the other hand, which is much lower. Here, one should note that as already discussed in [12] there is a systematic discrepancy between the helicity couplings of the $S_{11}(1535)$ extracted from pion photoproduction *versus* those from η-photoproduction. The latter ones are significantly larger. The $S_{11}(1535)$ dominates η-production but contributes only weakly to pion production which is dominated in this energy range by the $D_{13}(1520)$. Therefore, η-production is the better suited channel for the study of the $S_{11}(1535)$ properties. In the meantime the PDG proton coupling became dominated by the larger values from η-production, but the neutron coupling is still dominated by the small values from pion production. The resulting PDG neutron/proton ratio of the helicity couplings would correspond to a cross-section ratio for η-production in the S_{11} maximum of 0.26, which is unrealistic. The BoGa analysis finds a ratio of 0.79 and the simple BW fits a ratio of 0.68.

5.3.2 The region of the narrow peak in the $\gamma n \to n\eta$ reaction

In order to estimate the width of the narrow structure observed in the neutron data, the excitation function has been fitted up to $W \approx 1.8$ GeV with a purely phenomenological fit function. It is composed of the Breit-Wigner curve with energy-dependent width for the $S_{11}(1535)$ resonance and two further simple Breit-Wigner curves with constant width ($x \equiv 1$). The curves are compared to the data in fig. 24 and the fit parameters are listed in the

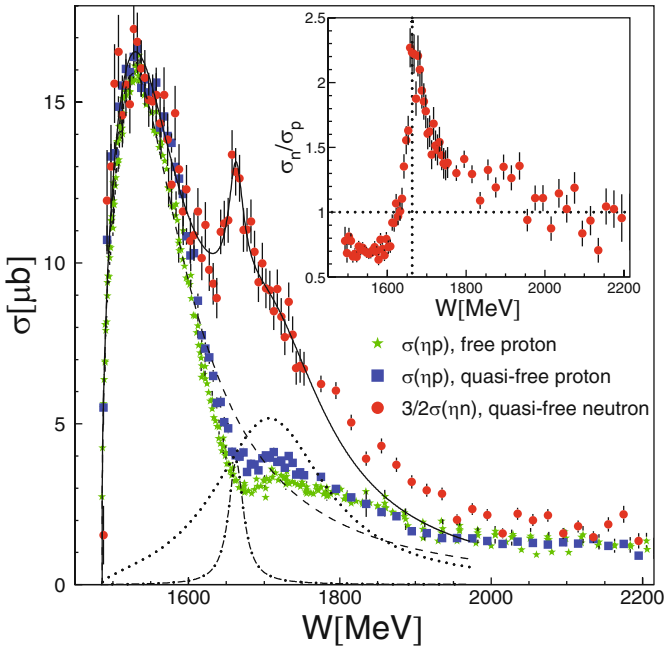

Fig. 24. Total cross-sections as a function of final-state invariant mass W for spectator momenta $p_S < 100\,\mathrm{MeV}$. Notation as in fig. 23. All curves for neutron data; dashed: fitted S_{11} line shape, dotted: broad Breit-Wigner resonance, dash-dotted: narrow Breit-Wigner, solid: sum of all.

bottom part of table 3. The parameters obtained for the S_{11} are consistent with the results discussed above. The broad BW curve located at $W \approx 1.7\,\mathrm{GeV}$ just serves for the effective parameterization of the excitation function. It subsumes contributions from all normally broad resonances in this energy region (such as $P_{11}(1710)$, $P_{13}(1720)$, $D_{15}(1650)$,...) as well as background components. The narrow Breit-Wigner curve at $W \approx 1.66\,\mathrm{GeV}$ has a FWHM of only $(25 \pm 12)\,\mathrm{MeV}$, on the same order as the experimental resolution of 25 MeV (FWHM). This width is somewhat dependent on the chosen parameterization, but also trials with different background shapes, *e.g.* of polynomial type, which result in a poorer fit quality, indicate a width below the 50 MeV level.

Since so far there is no information about the quantum numbers of this structure, in fact it is not even clear, whether it corresponds to a nucleon resonance, parameters like electromagnetic couplings cannot be given. However, if we treat the structure as a narrow S_{11} resonance the normalization of the fit corresponds to $A_{1/2} \cdot \sqrt{b_\eta} \approx 12 \times 10^{-3}\,\mathrm{GeV}^{-1/2}$.

The results for the angular dependence of the excitation functions are summarized in figs. 25, 26. Due to statistical limitations in the extraction process of the cross-sections depending on the final state W, the angular distributions are only coarsely binned. Figure 25 shows in the upper part excitation functions in dependence on W for four different bins of cm polar angles as well as the neutron/proton ratios. The bottom part shows the corresponding angular distributions for different bins of W. Finally, fig. 26 summarizes coefficients of the Legendre series of eq. (10), fitted to the angular distributions. The results are compared to free proton data and model calculations. The comparison to free proton data from the recent most precise measurement at MAMI [32] demonstrates impressively how well the elementary reaction on the free proton can be approximated by quasi-free data with W reconstructed from the $p\eta$ final-state kinematics. Significant deviations occur only very close to the production threshold, where the effects from Fermi motion are most pronounced. Comparing proton and neutron data, in particular the excitation functions for forward angles, it is even more apparent than in the total cross-section that the narrow structure observed in the neutron excitation function is accompanied by a pronounced dip in the proton data at the same position and of comparable width. It seems to be highly unlikely that these two structures are unrelated. This might indicate that some interference with a sign change between proton and neutron is involved. However, since the neutron peak and the proton dip are also visible in the total cross-section, at least part of this interference must be in the same partial wave. A dip-like structure has also been observed for comparable values of W in the $\pi^- p \to \eta n$ reaction, although at much lower statistical significance. As a possible explanation, similar to one version of the BoGa-model [55], the interference between the two S_{11} resonances was discussed in a K-matrix approach [75].

The comparison of the neutron data to model predictions leads to the following conclusions. Models which try to explain the structure observed in the Fermi smeared excitation function of the neutron data by one conventionally broad nucleon resonance like one of the scenarios in [55] are ruled out by the narrow width (see fig. 24) on the order of 25 MeV.

The coupled channel approach of Döring and Nakayama [53] shown in fig. 23 in fact produces a structure of similar width close to the observed position, although the exact shape is somewhat different. Since this model includes only s-wave contributions it cannot predict realistic shapes of angular distributions. Nevertheless, the fitted Legendre coefficients (see fig. 26) do at least not contradict the assumption that only s-waves are important. The peak-like structure is clearly seen only in A_0, which is proportional to the total cross section. From the higher coefficients only A_3 might show a little structure close by, albeit not statistically significant.

A direct comparison of the predictions of the MAID model [35] and the model from Shklyar *et al.* [51] to the angular distributions (see bottom part of fig. 25) shows that both models disagree with the neutron data throughout most of the energy range, in particular around the peak structure at $W \approx 1.67\,\mathrm{GeV}$. Agreement with the proton data is of course much better since free proton data have been used to fix the parameters of both models.

A more detailed comparison reveals some interesting features. The MAID model reproduces reasonably well the prominent structure in the ratio of neutron and proton cross-section in the forward angular range (upper part of fig. 25). However, even there it does not show any indication of the peak-like structure in the excitation function of

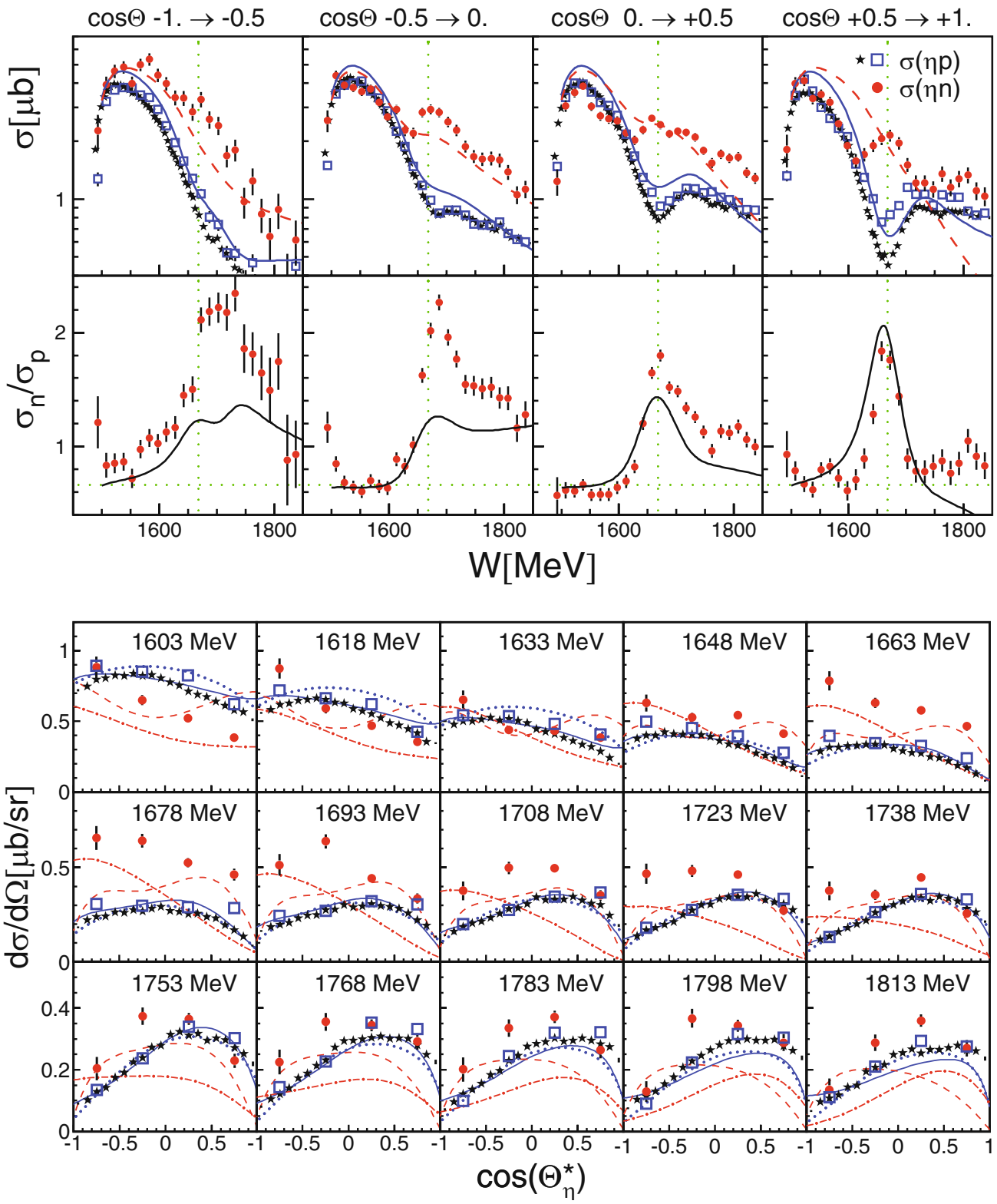

Fig. 25. Top, first row: excitation functions for different bins of η cm polar angle. (Blue) open squares: quasi-free proton data, (black) stars: free proton data from [32], (red) dots: quasi-free neutron data scaled up by 3/2. (Blue) solid lines: η-MAID [35] for the proton target, (red) dashed lines: η-MAID for the neutron target. Second row: ratio of neutron and proton cross-section for data and η-MAID. Vertical dotted lines: position of narrow peak in neutron data, horizontal dotted lines: $\sigma_n/\sigma_p = 2/3$. Bottom part: angular distributions. Same notation as top part (but neutron data not scaled); additional curves (blue) dotted: proton model from Shklyar *et al.* [51], (red) dash-dotted: neutron model from the same reference.

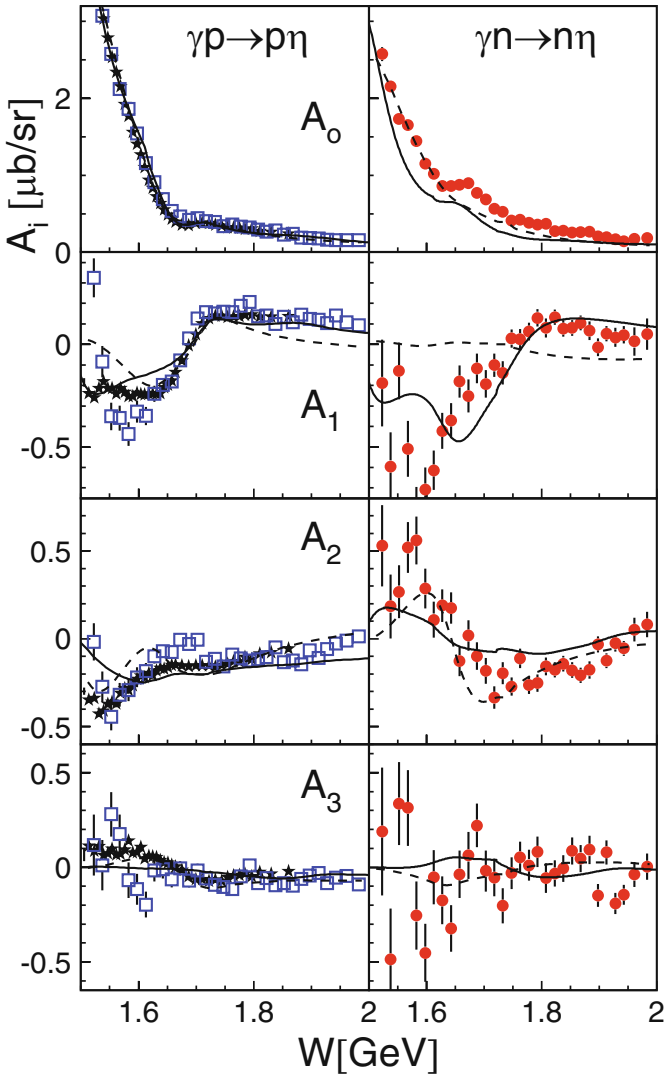

Fig. 26. Fitted coefficients of the Legendre series as a function of final-state invariant mass W. Left-hand side: (black) stars free proton, (blue) squares quasi-free proton. Right-hand side: (red) dots quasi-free neutron. Curves: dashed standard MAID model [35], solid: Shklyar *et al.* [51].

the $\gamma n \to n\eta$ reaction. The peak in the ratio stems alone from the dip in the proton cross-section. Since it is unlikely that these two structures are unrelated, this casts also some doubts whether the "dip" structure in the proton cross-section was correctly interpreted in this model. The comparison certainly rules out that the neutron structure can be entirely explained by a strong contribution of the $D_{15}(1675)$ resonance. A comparison of the fitted Legendre coefficients shows that the MAID model does not reproduce the peak in the A_0 coefficients and also fails completely for A_1, indicating that the strong S-P interference is not reflected in the model. On the other hand, the good agreement for the A_2 coefficient means that the S-D interference term (in particular the $S_{11}(1535)$-$D_{13}(1520)$ interference) is well understood. The Shklyar model [51] shows at least some indication for a peak in A_0 at the right position and is in much better agreement with A_1, although here it predicts a dip structure around $W \approx 1.67\,\mathrm{GeV}$, which is not in the data. Agreement with A_2 is not as good as for MAID. It is evident that the comparison of data and models does not allow a final conclusion about the nature of the structure in the neutron excitation function.

6 Summary and conclusions

Precise cross section data have been measured for quasi-free photoproduction of η-mesons off protons and neutrons bound in the deuteron. Due to the combined analysis of events in coincidence with recoil protons, recoil neutrons, and of the inclusive reaction systematic uncertainties related to the detection of the recoil nucleons could be reliably controlled. The results confirm earlier measurements in the region of the $S_{11}(1535)$ resonance and reveal an unexpected structure in the total cross-section of the $\gamma n \to n\eta$ reaction around incident photon energies of 1 GeV.

The results of an analysis based on the invariant mass of the η-proton pairs from quasi-free photoproduction off the proton are in excellent agreement with free proton data. This demonstrates that no nuclear effects beyond Fermi motion are involved and that these effects can be reliably removed by this method. An identical analysis of the quasi-free neutron data confirms a very narrow peak in the neutron excitation function around $W \approx 1.67\,\mathrm{GeV}$ with a width of only $\approx 25\,\mathrm{MeV}$ (FWHM), which seems to correspond to a dip-like structure in the proton excitation function at the same energy. The nature of this structures is not yet understood. Clearly ruled out are only single isolated resonances with conventional width like *e.g.* the $D_{15}(1675)$ in the MAID model. Scenarios with a narrow resonance or different types of coupled channel effects cannot yet be discriminated with the available data.

We wish to acknowledge the outstanding support of the accelerator group and operators of ELSA. We gratefully acknowledge stimulating discussions with D. Glazier concerning the analysis of the final state invariant mass and with M. Döring, V. Shklyar, and L. Tiator about the interpretation of the results. This work was supported by Schweizerischer Nationalfonds and the Deutsche Forschungsgemeinschaft (SFB/TR-16.)

References

1. S. Dürr *et al.*, Science **322**, 1224 (2008).
2. J. Bulava *et al.*, Phys. Rev. D **82**, 014507 (2010).
3. T. Burch *et al.*, Phys. Rev. D **74**, 014504 (2006).
4. S. Basak *et al.*, Phys. Rev. D **76**, 074504 (2007).
5. S. Capstick, W. Roberts, Prog. Part. Nucl. Phys. **241**, 241 (2000).
6. E. Klempt, J.M. Richard, Rev. Mod. Phys. **82**, 1095 (2010).
7. M. Anselmino *et al.*, Rev. Mod. Phys. **65**, 1199 (1993).
8. R. Bijker, F. Iachello, A. Leviatan, Ann. Phys. (N.Y.) **236**, 69 (1994).
9. N. Isgur, J. Paton, Phys. Rev. D **31**, 2910 (1985).

10. E.E. Kolomeitsev, M.F.M. Lutz, Phys. Lett. B **585**, 243 (2004).
11. V.D. Burkert, T.-S. Lee, Int. J. Mod. Phys. E **13**, 1035 (2004).
12. B. Krusche, S. Schadmand, Prog. Part. Nucl. Phys. **51**, 399 (2003).
13. R.G. Moorehouse, Phys. Rev. Lett. **16**, 772 (1966).
14. I. Jaegle *et al.*, Phys. Rev. Lett. **100**, 252002 (2008).
15. I. Jaegle *et al.*, Eur. Phys. J. A **47**, 11 (2011).
16. B. Krusche *et al.*, Phys. Rev. Lett. **74**, 3736 (1995).
17. J. Ajaka *et al.*, Phys. Rev. Lett. **81**, 1797 (1998).
18. A. Bock *et al.*, Phys. Rev. Lett. **81**, 534 (1998).
19. C.S. Armstrong *et al.*, Phys. Rev. D **60**, 052004 (1999).
20. R. Thompson *et al.*, Phys. Rev. Lett. **86**, 1702 (2001).
21. F. Renard *et al.*, Phys. Lett. B **528**, 215 (2002).
22. M. Dugger *et al.*, Phys. Rev. Lett. **89**, 222002 (2002).
23. V. Crede *et al.*, Phys. Rev. Lett. **94**, 012004 (2005).
24. T. Nakabayashi *et al.*, Phys. Rev. C **74**, 035202 (2006).
25. O. Bartalini *et al.*, Eur. Phys. J. A **33**, 169 (2007).
26. O. Bartholomy *et al.*, Eur. Phys. J. A **33**, 133 (2007).
27. D. Elsner *et al.*, Eur. Phys. J. A **33**, 147 (2007).
28. H. Denizli *et al.*, Phys. Rev. C **76**, 015204 (2007).
29. V. Crede *et al.*, Phys. Rev. C **80**, 055202 (2009).
30. M. Williams *et al.*, Phys. Rev. C **80**, 045213 (2009).
31. M. Sumihama *et al.*, Phys. Rev. C **80**, 052201(R) (2009).
32. E.F. McNicoll *et al.*, Phys. Rev. C **82**, 035208 (2010).
33. B. Krusche *et al.*, Phys. Lett. B **397**, 171 (1997).
34. A. Fantini *et al.*, Phys. Rev. C **78**, 015203 (2008).
35. W.-T. Chiang *et al.*, Nucl. Phys. A **700**, 429 (2002).
36. K. Nakamura *et al.*, J. Phys. G **37**, 075021 (2010).
37. V.A. Anisovich *et al.*, Eur. Phys. J. A **25**, 427 (2005).
38. B. Krusche *et al.*, Phys. Lett. B **358**, 40 (1995).
39. P. Hoffmann-Rothe *et al.*, Phys. Rev. Lett. **78**, 4697 (1997).
40. V. Hejny *et al.*, Eur. Phys. J. A **6**, 83 (1999).
41. J. Weiss *et al.*, Eur. Phys. J. A **16**, 275 (2003).
42. J. Weiss *et al.*, Eur. Phys. J. A **11**, 371 (2001).
43. M. Pfeiffer *et al.*, Phys. Rev. Lett. **92**, 252001 (2004).
44. N. Kaiser, P.B. Siegel, W. Weise, Phys. Lett. B **362**, 23 (1995).
45. N. Kaiser, T. Waas, W. Weise, Nucl. Phys. A **612**, 297 (1997).
46. M. Polyakov, A. Rathke, Eur. Phys. J. A **18**, 691 (2003).
47. R.A. Arndt *et al.*, Phys. Rev. C **69**, 035208 (2004).
48. H.-C. Kim *et al.*, Phys. Rev. D **71**, 094023 (2005).
49. V. Kuznetsov *et al.*, Phys. Lett. B **647**, 23 (2007).
50. F. Miyahara *et al.*, Prog. Theor. Phys. Suppl. **168**, 90 (2007).
51. V. Shklyar, H. Lenske, U. Mosel, Phys. Lett. B **650**, 172 (2007).
52. R. Shyam, O. Scholten, Phys. Rev. C **78**, 065201 (2008).
53. M. Döring, K. Nakayama, Phys. Lett. B **683**, 145 (2010).
54. A. Fix, L. Tiator, M.V. Polyakov, Eur. Phys. J. A **32**, 311 (2007).
55. V.A. Anisovich *et al.*, Eur. Phys. J. A **41**, 13 (2009).
56. V. Kuznetsov *et al.*, Phys. Rev. C **83**, 022201(R) (2011).
57. D. Husman, W.J. Schwille, Phys. Bl. **44**, 40 (1988).
58. W. Hillert, Eur. Phys. J. A **28**, 139 (2006).
59. D. Elsner *et al.*, Eur. Phys. J. A **39**, 373 (2009).
60. E. Aker *et al.*, Nucl. Instrum. Methods A **321**, 69 (1992).
61. R. Novotny, IEEE Trans. Nucl. Sci. **38**, 379 (1991).
62. A.R. Gabler *et al.*, Nucl. Instrum. Methods A **346**, 168 (1994).
63. G. Suft *et al.*, Nucl. Instrum. Methods A **538**, 416 (2005).
64. H. van Pee *et al.*, Eur. Phys. J. A **31**, 61 (2007).
65. I. Jaegle, PhD thesis, University of Basel (2007) (`http://jazz.physik.unibas.ch/site/theses.html`).
66. R. Brun *et al.*, GEANT, Cern/DD/ee/84-1 (1986).
67. T. Mertens *et al.*, Eur. Phys. J. A **38**, 195 (2008).
68. C. Zeitnitz *et al.*, The GEANT-CALOR interface user's guide (2001). (`http://www.staff.uni-mainz.de/zeitnitz/Gcalor/gcalor.html`)
69. E. Schäfer, PhD thesis, University of Mainz, unpublished (1993).
70. M. Lacombe *et al.*, Phys. Lett. B **101**, 139 (1981).
71. D. Elsner, Int. J. Mod. Phys. E **19**, 869 (2010).
72. W.T. Chiang *et al.*, Phys. Rev. C **68**, 045202 (2003).
73. K.H. Althoff *et al.*, Z. Phys. C **1**, 327 (1979).
74. A.M. Bernstein *et al.*, Phys. Rev. C **55**, 1509 (1997).
75. A.B. Gridnev, N.G. Kozlenko, Eur. Phys. J. A **4**, 187 (1999).